Computer Modeling in Engineering & Sciences

Tech Science Press

https://doi.org/10.32604/cmes.2026.081726

ARTICLE

Deep Learning-Assisted Modelling of Electro-Osmotic Flow in Thin Film Sutterby Hybrid Nanofluid over a Porous Inclined Sheet

Irfan Saif Ud Din[1], Imran Siddique[2,3,4,5], Zohaib Zahid[1], Muhammad Nadeem[6], Ibrahim Alraddadi[2,*] and Taha Radwan[7,*]

[1]Department of Mathematics, University of Management and Technology, Lahore, Pakistan
[2]Department of Mathematics, Faculty of Science, Islamic University of Madinah, Madinah, Saudi Arabia
[3]Department of Mathematics, University of Sargodha, Sargodha, Pakistan
[4]Research Center of Astrophysics and Cosmology, Khazar University, 41 Mehseti Street, Baku, Azerbaijan
[5]Jadara Research Center, Jadara University, Irbid, Jordan
[6]Mechanical Engineering Department DAMEC, Postgraduate Program in Mechanical and Materials Engineering PPGEM, Research Center for Rheology and Non-Newtonian Fluids CERNN, Soft Matter Research Center SOFMAT, Federal University of Technology Parana UTFPR, Curitiba, PR, Brazil
[7]Department of Management Information Systems, College of Business and Economics, Qassim University, Buraydah, Saudi Arabia

*Corresponding Authors: Ibrahim Alraddadi. Email: ialraddadi@iu.edu.sa; Taha Radwan. Email: t.radwan@qu.edu.sa

Received: 13 March 2026; Accepted: 20 April 2026; Published: 27 May 2026

ABSTRACT: This study examines the variable thermal conductivity and electroosmotic performance of Sutterby hybrid nanofluid (SBHNF) thin film flow over a stretched inclined sheet using an artificial neural network (ANN)-based on NARX (Multilayer Nonlinear Autoregressive Networks with Exogenous Inputs) multiple-layer backpropagation simulation with the Levenberg-Marquardt algorithm (LMA). AA7075 and AA7072 nanoparticles suspended in sodium alginate (SA) base fluid make up the hybrid nanofluid (HNF), which was selected due to its improved heat transfer properties and superior thermal conductivity. The model's practical applicability is enhanced by melting heat, nonlinear thermal radiation, boundary slip, and Newtonian heating effects, which are considered for surface heat flow. A dataset spanning three cases and seven scenarios of SBHNF is generated by solving the simplified governing equations using the built-in MATLAB bvp4c numerical methods. The dataset comprises three divisions: 80% allocated for training, 10% for validation, and 10% for testing. The proposed system is employed for the analysis of stream and thermal transmission, with conclusions validated by several approaches, including error histograms, regression plots, time series analysis, mean square error (MSE) of the loss function, autocorrelation, and cross-correlation. Findings from the AI-based LMA validate the suggested method for solving the SBHNF accurately. Joule heating, variable thermal conductivity, and other external sources elevate fluid temperature, whereas radiation heating markedly amplifies surface heat energy by accumulating, hence improving heat transfer. The opposing forces produced by magnetic fields, Darcy's law, and electro-osmosis reduce fluid velocity, which is effective for wellbore stability and hydraulic efficiency. The MSE and coefficient of determination (R^2) are used to assess the correctness and robustness of the suggested computational framework. The trained network indicated outstanding predictive accuracy with R^2 = 0.999 for all scenarios. The error histogram for the proposed model is 10^{-6} to 10^{-7}. The seven scenarios of SBHNF fall within the range of 10^{-8} to 10^{-13} for the attained high MSE (loss function) convergence levels.

KEYWORDS: Sutterby fluid; electro-osmosis effect; hybrid nanofluid; artificial neural network

1 Introduction

Nanofluids (NFs) are critical in industrial production, particularly in the creation of electrical and thermal devices. Because of their improved thermal and flow properties, NFs have drawn a lot of interest as nanotechnology has developed. Usually ranging in size from 10 to 100 nm, these fluids include nanoparticles scattered consistently throughout a base fluid. Mass-wise, the concentration of nanoparticles is usually kept between 1% and 5%. Metals, metal carbides, and carbon-based compounds are among the many components these nanoparticles could be made of. Nanofluids have found wide use in many scientific and industrial fields, including thermoelectric radiation retention, tailored pharmaceutical distribution methods, solar thermal collectors, geothermal energy systems, and cooling systems for hybrid engines, thanks in great part to their superior convective heat transfer capabilities [1,2]. Choi and Eastman [3] first presented the idea of nanofluids, that is, the addition of nanoparticles to traditional fluids to enhance thermal performance. Research later on has further enlarged this idea. Using many flow configurations and physical factors, Sajid et al. [4] investigated how nanoparticle suspensions affected fluid dynamics. Using nanoparticles of different geometries, that is, spherical, disc-shaped, and cylindrical, to increase thermal conductivity and heat production, Ali Khan et al. [5] scrutinized the peristaltic magnetohydrodynamic (MHD) flow of nanofluids. Cao et al. [6] investigated dynamic interactions with varied degrees of partial slip at the boundary surfaces between colloidal nanoparticles and water. Recently, by combining two or more distinct nanomaterials within a single base fluid, hybrid nanofluids (HNFs) exploit synergistic effects between different nanoparticle properties, yielding superior thermal performance compared to their single-nanoparticle counterparts. Examining HNF flow over various geometries, researchers have focused especially on linearly stretched surfaces highly important in industrial operations [7]. Optimizing thermal systems in geothermal energy systems, plastic sheet extrusion, high-power electronics, aerodynamic design, melt spinning, polymer processing, paint manufacture, solar thermal collectors, and glass fiber production depends on a knowledge of flow and heat transfer behavior throughout such domains [8]. For example, Afridi et al. [9] analyzed the behavior of HNF on a stretched sheet with different types of nanoparticles and important parameters. Jawad et al. [10] specifically analyzed melt heat transfer phenomena in stationary point flow conditions, while Nadeem et al. [11] specifically analyzed the heat transfer properties of a second-grade fuzzy HNF on a stretching surface with a permeability sheet. All such studies demonstrate that hybrid nanofluids/nanofluids play an increasingly important role in the advancement of engineering applications.

The analysis of Sutterby fluids has been an area with immense research efforts intended to address the enhancement of thermal efficiency for conventional base fluids. The non-Newtonian nature of these fluids has distinct rheological properties, which are remarkably useful in technical applications. The practical challenge is that most industrial fluids exhibit such non-Newtonian properties, and ignoring them leads to significant design errors in microfluidic devices, heat exchangers, and coating systems. Rehman et al. [12] worked on the massive enhancement of thermal efficiency achieved with the help of Sutterby nanofluids mixed with base fluid materials, which aims to facilitate intensified heat transfer. Nawaz [13] addressed the stability analysis related to small temperature changes in order to investigate the thermal performance of Sutterby nanofluids under various thermal gradient circumstances. Some studies have also aimed at understanding the role of temperature and electromagnetic effects on Sutterby fluid dynamics. The effects of magnetic field forces on the values of Sutterby non-Newtonian fluids have been studied by Bilal et al. [14], while Sabir et al. [15] conducted an exploration based on the Cattaneo-Christov heat flow equation to determine the effects of thermal radiation and an inclined magnetic field on Sutterby nanofluids. Song et al. [16] studied Marangoni convection for Sutterby nanofluids based on melting heat and solutal boundary constraints and hence widened the significance of these fluids with respect to applications in microfluidics and thermal systems. Meanwhile, Abbasi et al. [17] studied and explored the characteristics of Sutterby nanofluids inside

an inexpensive channel and hence emphasized the significance of these fluids to a constrained flow channel area with respect to effects on momentum and heat transfer values. In most cases, most industrial fluids exhibit non-Newtonian properties, which cannot be justifiably modeled using Newtonian laws. Such fluids comprise pseudoplastic and dilatant fluids, which exhibit shear thinning and shear thickening properties, respectively. Various mathematical models for non-Newtonian fluids have been formulated. Of these, the Sutterby fluid model has been remarkably useful owing to its ability to be applied to different conditions. The ability to take on different ranges within Newtonian, shear-thinning, and shear-thickening flows makes this model useful. Through an analysis of the heat and mass transfer characteristics for the Sutterby nanofluid in a rotating disk, Hayat et al. [18] demonstrated the decrease in the velocity of flows depending on the variations in materials. This study emphasized the effect of variations in materials on the dynamics of flows, which confirmed the application potential for Sutterby fluid models in advanced simulation processes.

Bio-microfluidics is a branch of biofluid mechanics that deals with the investigation and manipulation of minute amounts of biofluids using capillaries or microchannels. Biofluids include biological samples, urine, blood, and biological constituents. There is an electrokinetic principle called electro-osmosis that applies to the transport of a bulk fluid from or through a fluid conduit influenced by an electric field. This matter relates to fluid dynamics examination in bio-microfluidics. An electric double layer (EDL) is formed in electroosmotic transport when opposing ions are attracted to a solid surface by an interface charge created by an electrolyte solution. Applying an external electric field causes the net mobile charge in an ionic solution to undergo the Coulomb force, which in turn causes the fluid to move. The field of bio-microfluidics makes extensive use of this phenomenon to regulate the flow of fluids via microscopic channels. Some examples of bio-microfluidic devices that use electro-osmosis and EDL include micro-peristaltic pumps, proteomic chips, lab-on-chip systems, and micro total analysis systems. In various settings, several researchers have investigated these impacts. Tripathi et al. [19] investigated how electric and magnetic fields affected the peristaltic movement of bodily fluids. Hafez et al. [20] explored the Darcy-Forchheimer flow of Casson nanofluid across a stretched sheet, including viscous dissipation and electroosmotic forces (EOF). Narla et al. [21] investigated Electroosmotic flow-regulated peristaltic transport concerning the effect of entropy generation. Zaher et al. [22] reported the boundary layer of the Williamson fluid model with a gyrotactic microbe influenced by electro-osmotic force and non-Darcian flow. Riasat et al. [23] assessed the Debye-Hückel linearisation approach to analyse electroosmotic forces. The influence of a quadratically heated Riga plate and the analysis of electric potential using Gauss's law produce complex flow dynamics. Nadeem et al. [24] examined the electroosmotic influence on the transport of viscoelastic Williamson HNF flow via the thin needle. Joule heating and entropy formation were factors that Ranjit et al. [25] considered in their analysis of two-layered electroosmotic flow. Bilal et al. [26] precisely solved a micro parallel channel's entropy-based flow in electroosmotic magneto-nanofluids.

Intelligent computing approaches have garnered considerable interest from academics and scientists recently, owing to their efficacy in addressing complicated real-world challenges, especially those related to optimization. ANNs, a branch of computer intelligence, use heuristic methods to analyze data. An ANN has three layers: input, hidden, and output, each represented by artificial neurons. Shah et al. [27] scrutinized the MHD micropolar fluid flow with heterogeneous–homogeneous chemical processes and viscous dissipation using an ANN based on the NARX technique. Ilyas et al. [28] investigated their applications in NF modeling. Zeeshan et al. [29] enhanced MHD Casson ternary HNFs by computational intelligence, whereas Sabir et al. [30] created a Morlet wavelet neural network to address the Lane–Emden equation. Furthermore, Uddin et al. [31] examined intelligent networks for modeling thin-film flow. Ishaq et al. [32] presented a novel intelligent computing approach for viscoelastic Johnson–Segalman fluid, employing an ANN using TensorFlow. This method significantly improves precision and dependability in fluid dynamics applications.

Islam et al. [33] constructed an ANN-LMA framework to simulate magnetized hybrid Ag-TiO_2/EG-water nanofluid flow on a bi-directional surface, considering temperature-dependent viscosity and thermal conductivity. For training (70%), validation (15%), and testing (15%), a bvp4c-generated dataset. The model has an MSE of 10^{-10}–10^{-7}. Key findings: magnetic field increases vertical velocity in decreasing flow but decreases it in stretching flow; horizontal velocity is always decreased. The hybrid nanofluid demonstrated 45% thermal enhancement compared to 18.6% for 10% Ag mono-nanofluid. Yousuf Ali et al. [34] modelled radiative electroosmotic flow (EOF) in a hybrid nanofluid (TiO_2–Al_2O_3–Fe_3O_4 in 50:50 propylene glycol–water) as a non-Newtonian Sutterby fluid with gyrotactic microorganisms, and solved numerically by the shooting method. The backpropagated LMA-based ANN-BLMS has $R = 1.0$. The main finding: Trihybrid PGW fluid velocity grows with Helmholtz, electroosmotic, and Sutterby parameters, but decreases with magnetic force. Electroosmotic and Helmholtz characteristics reduce heat transport, whereas thermal radiation increases it. The thermal performance of a ternary HNF (Cu–TiO_2–SiO_2/water) across a symmetrically extending sheet was examined by Priyadharshini et al. [35]. To predict physical phenomena, a support vector machine (SVM) method was used. The method was validated by statistical measures for error evaluation. The ternary HNF outperforms HNFs in terms of thermal performance, according to the results. Din et al. [36] studied the impact of thin film Maxwell fluid flow over the porous inclined surface using an ANN.

In this study, the flow configuration being looked at is a steady, two-dimensional, incompressible, and axisymmetric flow of a Sutterby hybrid (AA7075 + AA7072/SA) nanofluid flow model (SNFFM) with thin film over an inclined extended sheet. This flow arrangement is evaluated under the influence of an electromagnetic field, electro-osmotic effects, Darcy-Forchheimer law, varying thermodynamic conductors, and Joule heating. Moreover, slip and melting heat are implemented at the boundary of the inclined extended sheet. The MATLAB built-in bvp4c algorithm is used to compute the governing mathematical equations. One of the most complicated and successful subfields of machine learning is known as neural networks, and it has been used in this study. These networks have often been believed to be capable of modeling data and producing positive outcomes. Artificial neural network (ANN) with Multilayer Nonlinear Autoregressive Networks with Exogenous Inputs (NARX) and the Levenberg-Marquardt Algorithmic (LMA) are employed for precise predictions and accuracy. It is beneficial since it can address error functions and develop more rapid convergence methods. The suggested AI-based ANN-NARX method possesses several distinctive qualities that set it apart from traditional methods. Table 1 provides a comparative overview of various research gaps. This research represents multi-physical features using the new presumptions listed below:

- The non-linear thermal radiation and heat transfer in SNFFM cycling through a stretched inclined sheet are studied with the help of an artificial intelligence (AI) based multiple-layer simulation and the LMA with backpropagation.
- The produced dataset is then sent into the SNFFM to examine its approximations using the AI-encapsulated abilities of the MLP-LMA method.
- Statistical evaluation methods such as fitness plot curves, regression, error analysis, and histogram error are used to show the effectiveness, validity, and correctness of the given system.
- Comparison of the accuracy of the reference numerical solution acquired and the computations produced by the ANN is also considered.
- Nonlinear radiation, changing thermal conductance, and Joule burning processes are employed to illustrate the enhancement in heat transfer.
- Melting heat and slip conditions are imposed on the boundary of the inclined sheet.
- Magnetic fields, electroosmosis, and the Darcy-Forchheimer law have been used to control the fluid flow.

Table 1: Analyze the literature to evaluate how the novel elements of the current investigation compare to previous findings.

Authors	Nonlinear Thermal Radiation	Sutterby Fluid	Electro-Osmotic Forces	Melting Heat	Thin Film Flow	ANN-NARX
Rehman et al. [12]	No	Yes	No	No	No	No
Din et al. [36]	Yes	No	Yes	Yes	Yes	Yes
Present	Yes	Yes	Yes	Yes	Yes	Yes

The inclined thin film sheets are very adaptable and have a wide range of uses in sectors including environmental control, food production, chemical processing, and medicines that need effective heat and mass transmission. In today's industrial processes, their capacity to lower energy consumption and improve process efficiency makes them extremely valuable.

2 Mathematical Formulation

Examine the suggested flow scenario that investigates the narrow-film dynamics of an unstable Sutterby hybrid nanofluid (AA7075 + AA7072/SA) over an inclined permeable layer influenced by electrostatic stresses. Boiling warmth, Joule heating, nonlinear thermal radiation, activation energy, slip condition, and dynamic thermal conduction are included in the heat transfer analysis. The axial x-direction is associated with the velocity field, represented by $U = (u(y,\ t),\ v(y,\ t), 0)$. The slender liquid film develops due to the stretching velocity $U_w = b_1 x\,(1 - a_1 t)^{-1}$ along the x-axis on a sloped surface at an inclination α, where a_1, and b_1 are fundamental constants (time^{-1}) and t represents time, as exemplified in Fig. 1. The width of this layer, denoted as $h(t)$, is defined by exact dimensional constants and varies over time. The film's thickness varies due to flow dynamics and external influences during stretching. The electromagnetic fields, which are permanent and similar in the longitudinal (y-axis) orientation, are identified as $B(t) = B_o\,(1 - a_1 t)^{-0.5}$. T_w and C_w, indicate the warmth and quantity concentrations at the walls, while T_∞ and C_∞ signify the ambient temperatures and concentration levels, respectively. Additionally, fixed regarding temperature and concentrations are indicated as T_o and C_o, respectively [12–18].

$$\frac{\partial u}{\partial x} + \frac{\partial v}{\partial y} = 0. \tag{1}$$

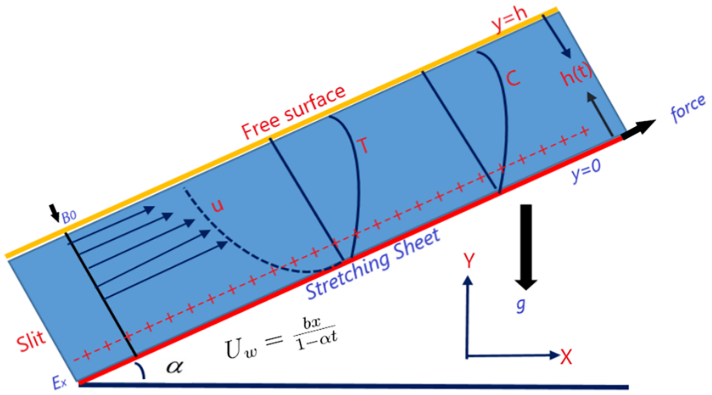

Figure 1: Flow geometry.

A Sutterby fluid is a non-Newtonian fluid with shear-thinning behavior, in which case its viscosity decreases with increasing shear rate. The flow dynamics, and consequently the velocity distribution, are governed by thin-filmed motion, the Darcy-Forchheimer rule, electrostatic effects, combined condensation, and exterior influences. Under the slip boundary conditions, the momentum equation controls the behavior of the Sutterby fluid in porous channels. While Nadeem et al. [24] and Bilal et al. [26] looked at electroosmotic effects. The created momentum equation for Sutterby fluids [14–19].

$$\frac{\partial u}{\partial t}+u\frac{\partial u}{\partial x}+v\frac{\partial u}{\partial y}=\frac{\mu_{hnf}}{\rho_{hnf}}\left(1-\frac{\beta_1^2}{6}\frac{\partial u}{\partial y}\right)^n\frac{\partial^2 u}{\partial y^2}-\frac{n\beta^2\mu_{hnf}}{6\rho_{hnf}}\left(1-\frac{\beta_1^2}{6}\frac{\partial u}{\partial y}\right)^{n-1}\frac{\partial u}{\partial y}\frac{\partial^2 u}{\partial y^2}-\frac{\nu_{hnf}u}{k^*}-\frac{C_k u^2}{\rho_{hnf}\sqrt{k^*}}$$
$$+P_eE_x-\frac{\sigma_{hnf}}{\rho_{hnf}}B_0^2u+\frac{g\left(\rho\beta\right)_{hnf}}{\rho_{hnf}}\left[\left(T-T_\infty\right)+\left(C-C_\infty\right)\right]\cos\alpha. \tag{2}$$

The energy equation that comprises nonlinear thermal radiation, variable thermal conductivity, Joule burning and thermal generation provides a robust foundation for examining temperature distribution inside a stream. Often employed in fields like environmental engineering, materials processing, solar energy, and combustion, this equation helps scientists and engineers ascertain how different thermal characteristics affect temperature profiles and heat transmission. The energy equation in the form of Cartesian coordinates is:

$$\frac{\partial T}{\partial t}+u\frac{\partial T}{\partial x}+v\frac{\partial T}{\partial y}=\frac{1}{\left(\rho Cp\right)_{hnf}}\frac{\partial}{\partial y}\left(k_{hnf}\left(T\right)\frac{\partial T}{\partial y}\right)+\frac{16\sigma^*}{3k_2\left(\rho Cp\right)_{hnf}}\frac{\partial}{\partial y}\left(T^3\frac{\partial T}{\partial y}\right)+\frac{\sigma_{hnf}}{\left(\rho Cp\right)_{hnf}}B_0^2u^2. \tag{3}$$

Mass transfer, influenced by energy and mass exchange, is crucial in fields such as fluid mechanics, microbiology, and airborne research, as it impacts particle mobility in a liquid medium with temperature variations. Activating energy is crucial in molecular kinetics, acting as the energy barrier that regulates reaction rates and affects processes like catalytic combustibility and nanomaterials construction.

$$\frac{\partial C}{\partial t}+v\frac{\partial C}{\partial y}+u\frac{\partial C}{\partial x}=D_m\frac{\partial^2 C}{\partial y^2}-{K_r}^2\left(C-C_\infty\right)\left(\frac{T}{T_\infty}\right)^{n_1}\exp\left(\frac{-E_a}{kT}\right). \tag{4}$$

Melting heat, the process through which a solid absorbs thermal energy and converts into a liquid, is a significant phenomenon in both industrial and natural systems. Regulated by heat transfer, it is essential in fields like material processing and environmental science. The slip condition affects fluid dynamics by facilitating movement along surfaces, which is essential in unconventional materials and structures with high-temperature gradients. Under these conditions, fluid movement across a melted substrate modifies velocity distributions and improves heat transfer efficiencies.

The boundary conditions (BCs) are [36]:

$$\left.\begin{aligned} &u=U_w+A\mu_{hnf}\frac{\partial u}{\partial y},-k_f\frac{\partial T}{\partial y}=\rho_f\left[L_1+C_m\left(T_w-T_\infty\right)\right]v,\quad C=C_w,\quad \text{at}\quad y=0,\\ &\frac{\partial u}{\partial y}=0,\frac{\partial T}{\partial y}=0,\frac{\partial C}{\partial y}=0,\frac{\partial h}{\partial t}=v,\qquad\qquad\qquad\qquad\qquad\qquad \text{at}\quad y=h\left(t\right), \end{aligned}\right\} \tag{5}$$

where A represents the slipping width or slip factor, with speed variables u and v oriented along the x-axis and y-axis, respectively. Additionally, L_1 denotes the potential heat of fusion, C_m represents the specific heat capacity of the material, C_k signifies the nonlinear drag coefficient, k^* indicates the permeation of the porous substance, μ_{hnf} refers to the flexible consistency of HNF, E_x is the electric field vector, and P_e means the regional electron frequency. ρ_{hnf} represents the density of HNF, δ^* is the Stefan-Boltzmann constant, k_2

signifies the mean absorption coefficient, k_{hnf} refers to the thermal conductivity of HNF, and β^2 Sutterby fluid coefficient.

Non-dimensional integers are predominantly utilised in liquid economics to obviate dependence on specific units of measurement, hence facilitating the analysis and comparison of fluid flow issues. This technique enables scientists and technicians to evaluate organisms of varying scales, gain a comprehensive grasp of the underlying physics, and extrapolate results to different scenarios or topologies. Dimensionalizing the governing equations of fluid dynamical issues facilitates analysis, optimisation, and scaling of solutions. Here η is a similarity variable, and the stream function (ψ) can be specified as $u = \partial\psi/\partial y$ and $v = -\partial\psi/\partial x$. By implementing the standardised matching parameters enumerated below

$$\left.\begin{aligned} &\eta = \sqrt{\frac{b_1}{\nu_f\left(1-a_1t\right)}}y,\ \ \psi = \sqrt{\frac{\nu_f b_1}{\left(1-a_1t\right)}}xF\left(\eta\right),\ \ T = T_\infty - T_0\left(\frac{b_1x^2}{\nu_f}\right)\left(1-a_1t\right)^{-3/2}\theta\left(\eta\right),\ \ \theta\left(\eta\right) = \frac{T-T_\infty}{T_w-T_\infty},\\ &C = C_\infty - C_0\left(\frac{b_1x^2}{\nu_f}\right)\left(1-a_1t\right)^{-3/2}\phi\left(\eta\right),\ \ u = \frac{b_1x}{1-a_1t}F'\left(\eta\right),\ \ v = -\sqrt{\frac{\nu_f b_1}{1-a_1t}}F\left(\eta\right),\ \ \phi\left(\eta\right) = \frac{C-C_\infty}{C_w-C_\infty}. \end{aligned}\right\} \tag{6}$$

Through a series of algebraic transformations, the governing Eqs. (2)–(5) can be converted into a system of ODEs, resulting in the following set of equations:

$$\begin{aligned} &\frac{\mu_r}{\rho_r}\left(1-\frac{\beta_s}{6}F''\right)^n F''' - \frac{\mu_r}{\rho_r}\frac{n\beta_s}{6}\left(1-\frac{\beta_s}{6}F''\right)^{n-1}F''F''' + FF'' - F'^2 - S\left(F' + \frac{\eta}{2}F''\right) - \frac{\delta_r}{\rho_r}MF'\\ &- \frac{\mu_r}{\rho_r}KpF' + Uhsme^2e^{-me\eta} + \left(\beta_T\right)_r\left(\alpha_1\theta + \alpha_2\phi\right)\cos\alpha = 0, \end{aligned} \tag{7}$$

$$\begin{aligned} &\frac{k_r}{\left(\rho Cp\right)_r}\left(\left(1+\delta\theta\right)\theta'' + \delta\theta'^2\right) + \Pr F\theta' - 2\Pr F'\theta - \frac{\Pr S}{2}\left(3\theta + \eta\theta'\right) + \Pr EcM\frac{\delta_r}{\left(\rho Cp\right)_r}\left(F'\right)^2\\ &+ \frac{N_r}{\left(\rho Cp\right)_r}\left(1+\theta\left(\theta_w-1\right)\right)^3\theta'' + \frac{3N_r}{\left(\rho Cp\right)_r}\left(\theta_w-1\right)\left(1+\theta\left(\theta_w-1\right)\right)^2\left(\theta'\right)^2 = 0, \end{aligned} \tag{8}$$

$$\phi'' + Sc\left(F\phi' - 2F'\phi - \frac{S}{2}\left(3\phi + \eta\phi'\right)\right) + 2KSc\phi\left(1+\gamma_c\theta\right)^{n_1}\mathrm{e}^{\left(\frac{-E}{1+\gamma_c\theta}\right)} = 0. \tag{9}$$

The transformed boundary conditions (BCs) are:

$$\left.\begin{aligned} &F\left(\eta\right) = 0, F'\left(\eta\right) = 1 + \lambda\mu_r F''\left(\eta\right),\ \ \Pr F\left(\eta\right) + Me\theta'\left(\eta\right) = 0,\ \ \phi\left(\eta\right) = 1, \quad \text{at} \quad \eta = 0,\\ &F\left(\eta\right) = \frac{S\beta}{2}, F''\left(\eta\right) = 0,\ \ \theta'\left(\eta\right) = 0,\ \ \phi'\left(\eta\right) = 0, \qquad\qquad\qquad \text{at} \quad \eta = \beta. \end{aligned}\right\} \tag{10}$$

The following are the non-dimensional factors that were shown:

$$\left.\begin{aligned} &S = \frac{a_1}{b_1},\ \Pr = \frac{\mu_f C_p}{k_f},\ Kp = \frac{\nu_f}{b_1k^*},\ Gr = \frac{g\left(T_w-T_\infty\right)x^3\left(\beta_T\right)_f}{\nu_f^2},\ M = \frac{B_0^2\sigma_f}{b_1\rho_f},\ Fr = \frac{C_k}{\sqrt{k^*}},\\ &\theta_w = \frac{T_w}{T_\infty},\ Gc = \frac{g\left(C_w-C_\infty\right)x^3\left(\beta_c\right)_f}{\nu_f^2},\ Uhs = \frac{\varepsilon_0\varepsilon K_BTE_x}{eZ},\ \beta = \sqrt{\frac{b_1}{\nu_f\left(1-a_1t\right)}}h\left(t\right),E = \frac{E_a}{k_1^*T_\infty},\\ &Me = \frac{C_m\left(T_\infty-T_w\right)}{L_1 + C_m\left(T_w-T_o\right)},\ \gamma_c = \frac{T_w-T_\infty}{T_\infty},\lambda = A\sqrt{\frac{b_1}{\nu_f\left(1-a_1t\right)}},N_r = \frac{16\delta^*T_\infty^3}{3k_fk_2},Ec = \frac{U^2}{C_p\left(T_w-T_\infty\right)},\\ &\mathrm{Re}_x = \frac{U_wx}{\nu_f},\alpha_1 = Gr\left(\mathrm{Re}_x\right)^{-2},m_e^2 = \frac{\nu_f\left(1-a_1t\right)}{b_1\lambda_e^2},\ \alpha_2 = Gc\left(\mathrm{Re}_x\right)^{-2},\beta_s = \beta_1^2b_1\sqrt{\mathrm{Re}_x}, \end{aligned}\right\} \tag{11}$$

where S, Pr, α_1, α_2, M, Uhs, Kp, β, Me, E, Ec, β_s, and θ_w dimensionless unsteady parameter, Prandtl number, Thermally Grashof number, Solutal Grashof number, electromagnetic parameters, Helmholtz-Smoluchowski motion, permeable coefficient, film width, melting heat factor, activated energy, temperature differential, thermally radiation, Eckert amount, fluid variable, and temperature conversion characteristic. Furthermore, the relationship between temperature and thermal conductivity $(k(T))$ of liquid metal has been studied. The liquid metals' thermal conductivity is nearly a linear function of temperature between 0°F and 400°F. $(k(T)) = a_\infty(1+\delta\theta)$ is the assumed value of thermal conductivity. In addition, the constant heat conductivity is represented as a_∞ as $\eta \to \infty$. Table 2 presents an extensive compilation of nanoparticles, such as AA7072, AA7075, and Sodium Alginate (SA), utilized as the base fluid, along with various thermophysical properties. Meanwhile, Table 3 illustrates the correlation characteristics of hybrid nanofluids. The necessary hybrid nanofluid is formulated by dispersing AA7072 and AA7075 nanoparticles within the base fluid SA.

Table 2: Physical properties of micro-sized particles and base fluid [24].

Characteristics	$\rho\,(\mathrm{kg/m^3})$	C_p (J/kgK)	k (W/mK)	σ (S/m)
SA	989	4175	0.6376	2.6×10^{-4}
AA7072	2720	893	222	34.83×10^{6}
AA7075	2810	960	173	26.77×10^{6}

Table 3: Thermo-physical properties of nanofluid and HNF [24].

Property	Nanofluid	Hybrid Nanofluid
Density	$\rho_q = \rho_{nf}/\rho_f = (1-\phi_1) + \rho_{s1}\phi_1/\rho_f$	$\rho_q = \frac{\rho_{hnf}}{\rho_f} = \left((1-\phi_1) + \phi_1\rho_{s1}/\rho_f\right)(1-\phi_2) + \phi_2\rho_{s2}/\rho_f$
Heat capacity	$(\rho c_p)_q = (\rho c_p)_{nf}/(\rho c_p)_f = (1-\phi_1) + \phi_1\rho_{s1}/(\rho c_p)_f$	$(\rho c_p)_q = (\rho c_p)_{hnf}/(\rho c_p)_f = \phi_2(\rho c_p)_{s2}/(\rho c_p)_f + \left((1-\phi_1) + \phi_1(\rho c_p)_{s1}/(\rho c_p)_f\right)(1-\phi_2)$
Dynamic viscosity	$\mu_q = \mu_{nf}/\mu_f = (1-\phi_1)^{-2.5}$	$\mu_q = \mu_{hnf}/\mu_f = (1-\phi_1)^{-2.5}(1-\phi_2)^{-2.5}$
Thermal conductivity	$\frac{k_{nf}}{k_f} = \frac{k_{s1} + k_f(n-1) - \phi_1(n-1)(k_f - k_{s1})}{k_{s1} + k_f(n-1) + \phi_1(k_f - k_{s1})}$	$k_q = \frac{k_{hnf}}{k_{nf}} = \frac{k_{s2} + k_{nf}(n-1) - \phi_2(n-1)(k_{nf} - k_{s2})}{k_{s2} + k_{nf}(n-1) + \phi_2(k_{nf} - k_{s2})}$
Electric conductivity	$\frac{\sigma_{nf}}{\sigma_f} = \frac{\sigma_{s1} + \sigma_f(n-1) - (n-1)(\sigma_f - \sigma_{s1})\phi_1}{\sigma_{s1} + \sigma_f(n-1) + (\sigma_f - \sigma_{s1})\phi_1}$	$\sigma_q = \frac{\sigma_{hnf}}{\sigma_{nf}} = \frac{\sigma_{s2} + \sigma_{nf}(n-1) - (n-1)(\sigma_{nf} - \sigma_{s2})\phi_2}{\sigma_{s2} + \sigma_{nf}(n-1) + (\sigma_{nf} - \sigma_{s2})\phi_2}$

2.1 For Electro-Osmotic Flow

The given differential equation is [19–26]:

$$\frac{d^2\overline{\Gamma}}{dy^2} = \frac{1}{\lambda_e^2}\overline{\Gamma}, \tag{12}$$

where $\lambda_e = (eZ_v)^{-2\frac{\varepsilon T_a \nu K_B}{2n_0}}$. The dimensionless variables are introduced as:

$$\Gamma = \frac{\overline{\Gamma}}{\xi},\ \eta = \sqrt{\frac{b_1}{\nu_f(1-a_1 t)}}\,y, \tag{13}$$

here ξ is a scaling factor for $\overline{\Gamma}$, and η is a rescaled version of y.

$$\frac{d^2\Gamma}{d\eta^2} = m_e^2\Gamma. \tag{14}$$

The equation seems to use $\Gamma \to \infty$ but gives $\Gamma = e^{-m_e^2\eta}$, which suggests a typo in the boundary condition or the solution. Assuming $\Gamma \to 0$ as $\eta \to \infty$ is more reasonable. Here, $m_e^2 = \frac{\nu_f(1-a_1 t)}{b_1\lambda_e^2}$ (assuming m_e is positive).

2.2 Physical Quantities

The skin frictional component, heat transmission, and mass transport ratios are the three most critical aspects of this subject in automotive and agricultural processes. The skin resistance coefficient can be quantitatively represented as [12–18]:

Skin Friction

$$Cf_x = \frac{\mu_{hnf}}{\rho_f {U_w}^2}\left[1 - \frac{\beta_1^2}{6}\frac{\partial u}{\partial y}\right]^n \frac{\partial u}{\partial y}\bigg|_{y=0}. \tag{15}$$

The dimensionless version of the aforementioned equation using Eq. (6) is

$$Cf_x\,(\mathrm{Re}_x)^{\frac{1}{2}} = \mu_r\left(1 - \frac{\beta_s}{6}F''(0)\right)^n F''(0). \tag{16}$$

Local Nusselt Number

The correlation of heat transit rate may be expressed mathematically as follows:

$$Nu_x = -\frac{-x}{k_f\,(T_w - T_\infty)}\left[k_{hnf}\,(T)\frac{\partial T}{\partial y} + \frac{16\sigma^* T_\infty^*}{3k^*}\frac{\partial T}{\partial y}\right]_{y=0}. \tag{17}$$

The aforementioned equation is represented as Eq. (6).

$$Nu_x\,(\mathrm{Re}_x)^{-0.5} = -\left(k_r\,(1+\varepsilon\theta\,(0)) + N_r\,(1+\theta\,(0)\,(\theta_w - 1))^3\right)\theta'(0). \tag{18}$$

Sherwood Number

The mass transfer rate coefficient can be interpreted mathematically as follows:

$$Sh_x = \frac{-x}{(C_w - C_\infty)}\left(\frac{\partial C}{\partial y}\right)_{y=0} \tag{19}$$

The non-dimensional version of the calculation above is given by Eq. (6).

$$(\mathrm{Re}_x)^{\frac{-1}{2}}\,Sh_x = -\phi'(0). \tag{20}$$

2.3 Numerical Solution

Finding precise solutions to the exceedingly chaotic flow equations that drive the NNF model is a tough task due to their complexity. This kind of problem may therefore be solved computationally using the numerical strategy Bvp4c (MATLAB) application. Several new factors are interpreted as follows, and the present problem is reduced to a set of connected first-order equations [7–9]:

$$F = z_1,\ \ F' = z_2,\ \ F'' = z_3,\ \ F''' = z_{3,}',\ \theta = z_4,\ \ \theta' = z_5, \theta'' = z_5',\ \ \phi = z_6,\ \ \phi' = z_7, \phi'' = z_8', \tag{21}$$

$$z_5' = \frac{(\rho Cp)_r}{k_r\left(1+\delta z_4\right) + N_r\left(1 + z_4\left(\theta_w - 1\right)\right)^3} \tag{22}$$

$$\left(\begin{array}{l} -\dfrac{k_r}{(\rho Cp)_r}\delta z_5 - \Pr z_1 z_5 + 2\Pr z_2 z_4 + \dfrac{\Pr S}{2}\left(3z_4 + \eta z_5\right) \\ -\Pr EcM\dfrac{\delta_r}{(\rho Cp)_r}\left(z_2\right)^2 - \dfrac{3N_r}{(\rho Cp)_r}\left(\theta_w - 1\right)\left(1 + z_4\left(\theta_w - 1\right)\right)^2\left(z_5\right)^2 \end{array}\right), \tag{21}$$

$$z_7' = -Sc\left(z_1 z_8 - 2z_2 z_7 - \frac{S}{2}\left(3z_7 + \eta z_7\right)\right) - 2\alpha_c Scz_7\left(1 + \gamma_c z_4\right)^n \mathrm{e}^{\left(\frac{-E}{1+\gamma_c z_4}\right)}. \tag{23}$$

BCs

$$\left.\begin{array}{l} z_1\left(\eta\right) = 0, z_2\left(\eta\right) = 1 + \lambda z_3\left(\eta\right),\ \ \Pr z_1\left(\eta\right) + Mez_5\left(\eta\right) = 0, z_7\left(\eta\right) = 1, \quad \text{at} \quad \eta = 0, \\ z_1\left(\eta\right) = \dfrac{S\beta}{2}, z_3\left(\eta\right) = 0, z_5\left(\eta\right) = 0, z_7\left(\eta\right) = 0, \qquad\qquad \text{at} \quad \eta = \beta. \end{array}\right\} \tag{24}$$

The skin friction and Nusselt number are altered by less than 0.01% when the mesh is refined from 50 to 200 points or when the tolerance is tightened from 10^{-6} to 10^{-8}. This substantiates the fact that the bvp4c solutions are mesh-independent and numerically convergent, as shown in Table 4.

Table 4: Grid analysis for skin friction and Nusselt number with tolerance.

Mesh Points	Tolerance	Skin Friction	Nusselt Number	Relative Change (%)
50	10^{-6}	−1.6506	5.2832	—
100	10^{-6}	−1.6506	5.2832	<0.01
200	10^{-6}	−1.6506	5.2832	<0.01
50	10^{-8}	−1.6506	5.2832	<0.001
100	10^{-8}	−1.6506	5.2832	—

3 Artificial Neural Networks

Artificial intelligence (AI) techniques, especially neural networks, have recently become significantly more popular in scientific research as a practical research tool. This facilitates the investigation and forecasting of various physical situations, supporting intricate fluid dynamics analysis. Performance metrics, gradient descent optimization for training, and the creation of an ANN structure are all part of the strategy. After finalizing the selection and formation of the sample dataset, normalization is necessary to rectify the disparate scales of various input parameters, as shown in Table 5. Eq. (25) standardizes several parameters to the [0, 1] interval, thereby promoting stable and effective model training. This technique mitigates the impacts

of dimensions and scale discrepancies, guaranteeing that all features maintain equivalent weights. Thus, it inhibits the model from forming preferred biases stemming from fluctuations in the numerical ranges of its parameters. The normalizing process significantly improves the model's stability and the comparability of outcomes [27–36].

$$y = \frac{x_i - x_{\min}}{x_{\max} - x_{\min}}, \tag{25}$$

where, the sample parameter variable is represented by x_i, the normalized result by y, and the sample parameter variable's maximum and minimum values by $x_{\max}$ and $x_{\min}$, respectively.

Table 5: Presentation of seven distinct scenarios for each of the three instances of SNFFM.

Cases	Uhs	Kp	M	θ_w	β_s	S	Sc	Scenarios
1	0.5	0.4	0.3	1.2	0.3	1.0	1.5	
2	1.0	0.4	0.3	1.2	0.3	1.0	1.5	I
3	1.5	0.4	0.3	1.2	0.3	1.0	1.5	
1	0.2	0.3	0.3	1.2	0.3	1.0	1.5	
2	0.2	0.6	0.3	1.2	0.3	1.0	1.5	II
3	0.2	0.9	0.3	1.2	0.3	1.0	1.5	
1	0.2	0.4	0.1	1.2	0.3	1.0	1.5	
2	0.2	0.4	0.5	1.2	0.3	1.0	1.5	III
3	0.2	0.4	1.0	1.2	0.3	1.0	1.5	
1	0.2	0.4	0.3	1.1	0.3	1.0	1.5	
2	0.2	0.4	0.3	1.3	0.3	1.0	1.5	IV
3	0.2	0.4	0.3	1.5	0.3	1.0	1.5	
1	0.2	0.4	0.3	1.2	1.1	1.0	1.5	
2	0.2	0.4	0.3	1.2	1.5	1.0	1.5	V
3	0.2	0.4	0.3	1.2	2.0	1.0	1.5	
1	0.2	0.4	0.3	1.2	0.3	0.3	1.5	
2	0.2	0.4	0.3	1.2	0.3	0.6	1.5	VI
3	0.2	0.4	0.3	1.2	0.3	0.9	1.5	
1	0.2	0.4	0.3	1.2	0.3	1.0	1.1	
2	0.2	0.4	0.3	1.2	0.3	1.0	1.5	VII
3	0.2	0.4	0.3	1.2	0.3	1.0	2.0	

After that, the Non-Newtonian SBHNF was addressed through a multi-layer perceptron (MLP) that predicts with backpropagation and NARX (Nonlinear Autoregressive with Exogenous Inputs). A NARX network is a kind of recurrent dynamic neural network that integrates memory via time-delayed feedback from its prior outputs (autoregressive terms) and external input signals (exogenous terms) to forecast current outputs. NARX networks, in contrast to conventional feedforward networks that immediately associate inputs with outputs without memory, are adept at modelling nonlinear, time-dependent dynamical systems like fluid flows, since they preserve knowledge about previous states via internal feedback loops and temporal delays. The NARX was used for this investigation because it can mimic the dynamic, time-dependent Sutterby HNF thin film flow. The NARX model excels at handling complicated nonlinear governing

equations, including changing thermal conductivity, nonlinear radiation, and the Sutterby fluid's shear-thinning features. The NARX network converges quickly and reliably, making it a strong surrogate model tool with the Levenberg-Marquardt Algorithm (LMA). The LMA was integrated with MLP to efficiently address the problem's complexity. This model, which has one input layer, two hidden layers containing 10, 10 neurons, and one output layer, is set up to support sequential input. The changeable weights in the hidden layers are used to identify patterns and connections in the data. Furthermore, the sigmoid nonlinear activation function is used to allow the model to learn complex associations. Gradient descent optimization is used in training when weights are iteratively changed to minimize prediction error. With each iteration, backpropagation improves accuracy by modifying these weights in response to variations between actual and expected outputs. Several key elements are adjusted to improve training efficiency, including hyperparameter tuning, convergence criteria, and learning rate adaptation. The output layer iteratively minimizes errors before producing predictions. The method starts with the creation of a dataset using SBHNF settings and the identification of the key variables. The dataset is created by solving the ODE system in MATLAB using the bvp4c solver (relative tolerance 10^{-6}, absolute tolerance 10^{-8}). Each parameter combination in Table 5 is discretized into 101 evenly spaced points in the spatial domain $\eta \in [0, \beta = 1]$ (where β is the film thickness). The dataset contains 2121 samples from all seven scenarios and three cases (21 parameter combinations, each giving 101 geographical points). Randomly shuffling the dataset divides it into three mutually exclusive subsets: 80% for training (1697 samples), 10% for validation (212 samples), and 10% for testing. The ANN is trained with the training dataset, and the gradient of the MSE loss function is calculated, and the training parameters are updated by gradient descent optimization. To lower the error, the weights are changed, and the procedure is repeated until convergence. The computational setup included MATLAB R2025b (Deep Learning Toolbox version 14.5) operating on an Intel Core i7-10750H CPU @ 2.60 GHz with 32 GB RAM and a 64-bit operating system; the average training duration per model varied from 1 to 2 s. The precision and efficacy of the proposed system are dictated by the assessment, instruction, and validation procedures integrated into the neural network's design, as shown in Fig. 2. Especially in addressing the SNFFM, the LMA method shows notable variations from conventional methods. Along with efficient mapping between input and output variables, this global modeling technique helps create comprehensive diagnostic graphs. Seven scenarios (Table 5) delineated by the fluid system, with fluctuations in the Helmholtz-Smoluchowski velocity (Uhs), porosity parameter (Kp), magnetic parameter (M), temperature ratio parameter (θ_w), fluid parameter (β_s), unsteady parameter (S), and Schmidt number (Sc) for each case. The other parameters are fixed for all seven scenarios.

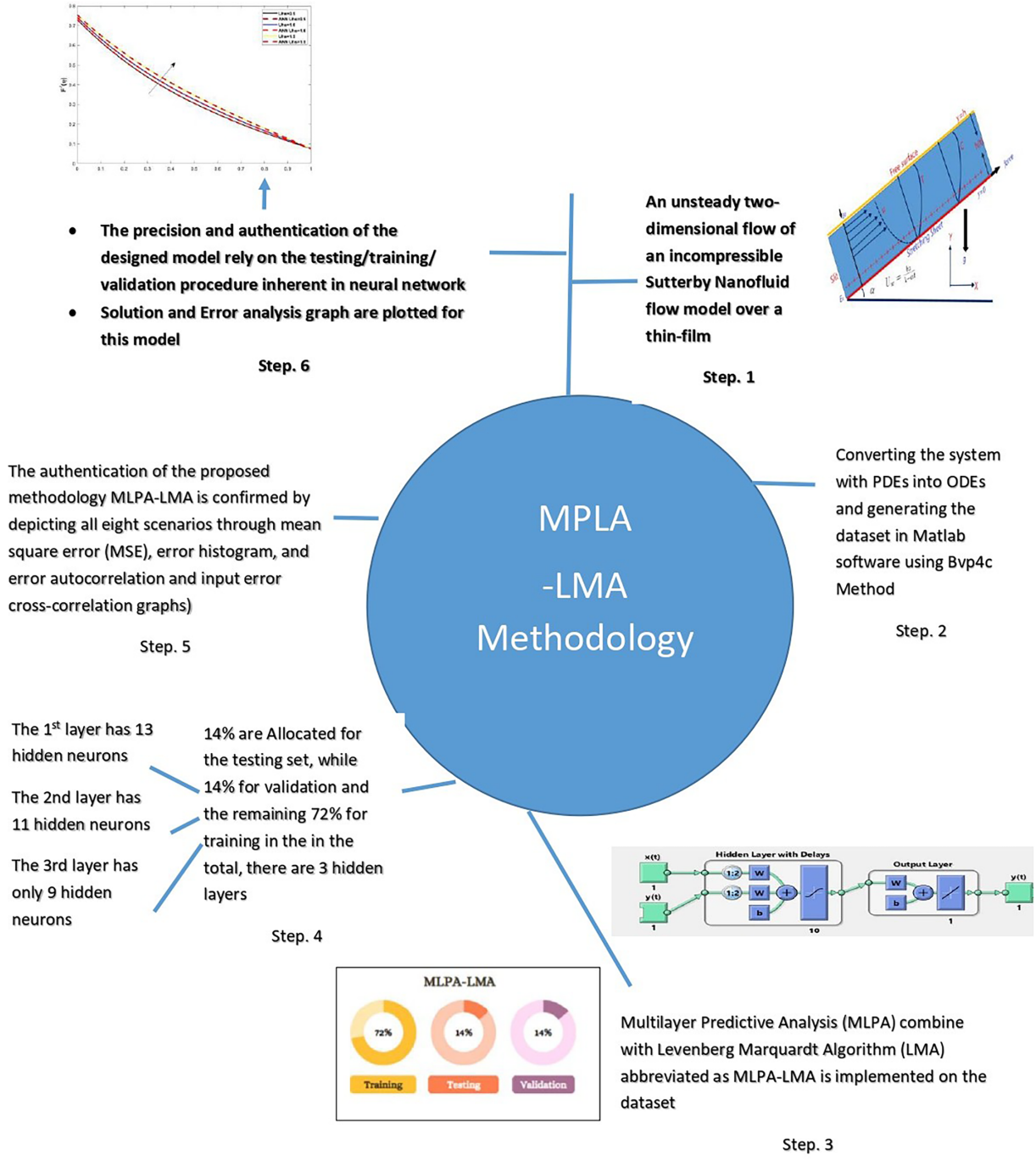

Figure 2: Flowchart of the complete process for model evaluation.

4 Results and Discussion

This section presents a comprehensive study of unsteady Sutterby hybrid (AA7075 + AA7072/SA) nanofluid flow with thin film across a starching porous sheet using the ANN-NARX approach, taking into account the effects of variable thermal conductivity, nonlinear thermal radiation, electroosmotic effect, and melting heat. The impacts of distinct parameters on velocity, temperature, and concentration are discussed. The parameter values are set to Pr = 16.37, $\delta = 0.4$, $N_r = 0.3$, $\theta_w = 1.1$, $S = 0.5$, $Kp = 0.4$, $\alpha = 0.5$,

$Uhs = 0.3$, $\alpha_1 = 0.3$, $K = 0.5$, $Me = 0.2$, $\alpha_2 = 0.4$, $\gamma_c = 0.3$, $E = 0.5$, $\alpha_c = 0.5$, $\lambda = 0.2$, $n = n_1 = 0.5$, $\beta_s = 0.6$, $M = 0.2$, $m_e = 0.3$, and $Sc = 1.5$, as default settings. The bvp4c technique in MATLAB is employed for computing the ODEs (7)–(9) as well as BCs (10). The current research comprises a range of non-dimensional factors whose relevance is clear based on current literature.

4.1 Performance Graphs

The efficiency graph is a trained slope employed to monitor the development of an ANN-NARX. A consistent decline in the MSE loss function over epochs signifies that the model is acquiring knowledge efficiently. The forecasts are becoming more accurate and nearing the exact goal measurements, while the framework is systematically decreasing predicted inaccuracy as instruction progresses. This situation is often favourable, signifying that optimisation is advancing successfully in the model, leading to enhanced efficiency. Figs. 3a–9a depict the performance of the seven scenarios. The convergence of the specified scheme ANN-NARX with LMA was achieved at 79, 79, 53, 96, 90, 35, and 29 epochs, corresponding to approximately 8.2975×10^{-11}, 5.6319×10^{-11}, 2.7988×10^{-13}, 4.4911×10^{-11}, 6.9489×10^{-11}, 1.5598×10^{-10}, and 2.5735×10^{-11}, accordingly. Furthermore, the proposed model exhibits fewer differences between the actual and projected values, which indicates better model performance and a lower MSE loss function. Testing and validation loss curves show that the model is proficient in forecasting results for particular setups. In terms of physicality, a lower MSE loss function means that the model is performing very well in tracking the expected physical trend of the system. Consistently low errors over the whole computational domain demonstrate the model's good generalization beyond the training data. The ANN-NARX model effectively learns the underlying physics, making it a reliable substitute for expensive numerical simulations, as confirmed by its quick convergence and ultralow MSE values $\left(10^{-10}-10^{-13}\right)$.

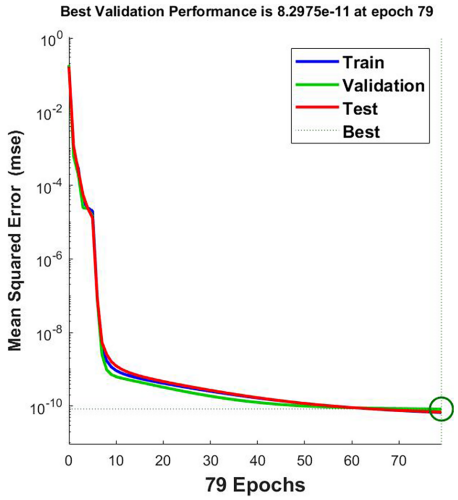

(a). MSE loss function

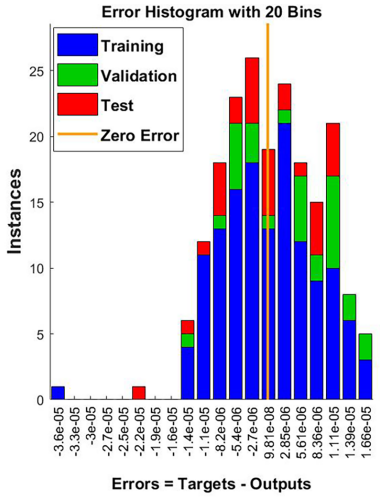

(b). Error histogram

Figure 3: (Continued)

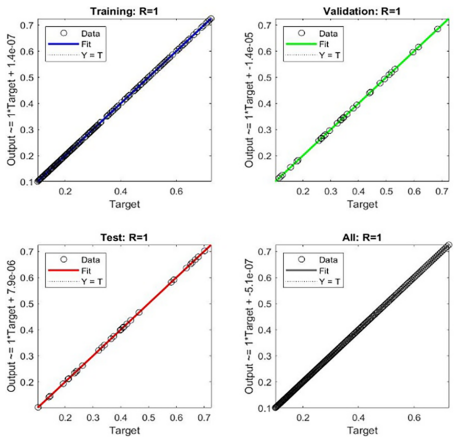

(c). Regression

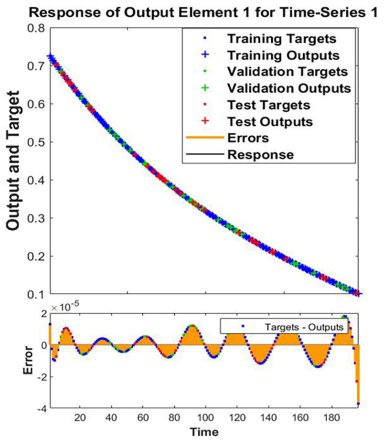

(d). Time Series Response

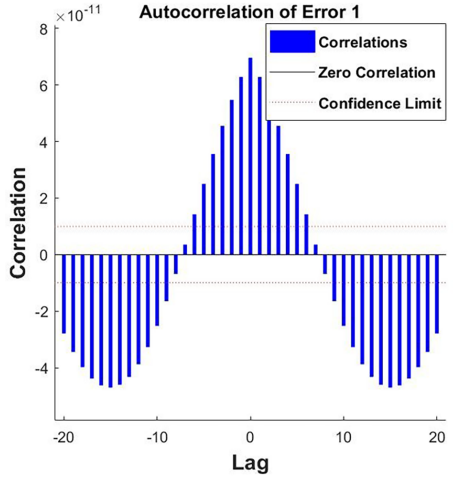

(e). Error Autocorrelation

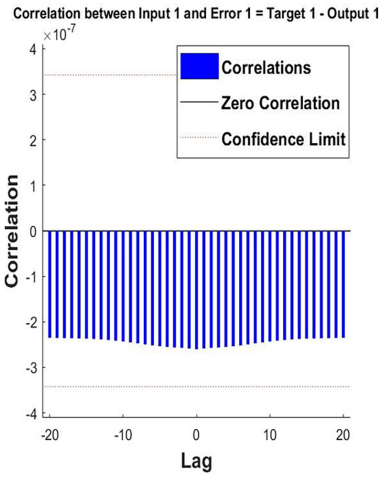

(f). Input Error Cross Correlation

Figure 3: (**a**–**f**): Performance of ANN-NARX for scenario I.

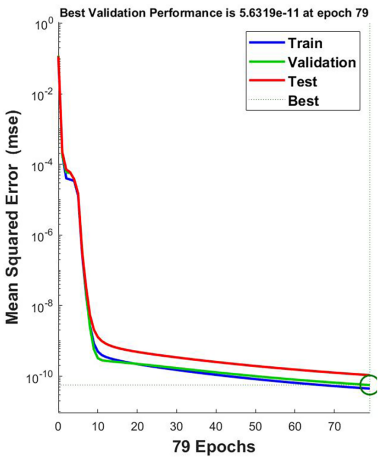

(a). MSE loss function

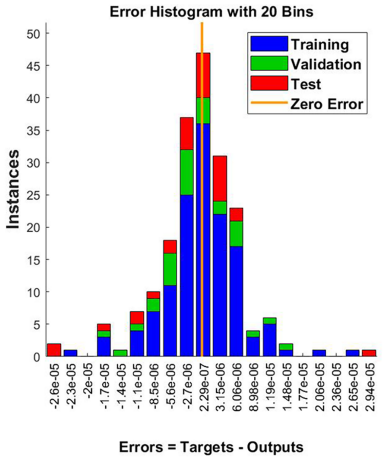

(b). Error Histogram

Figure 4: (Continued)

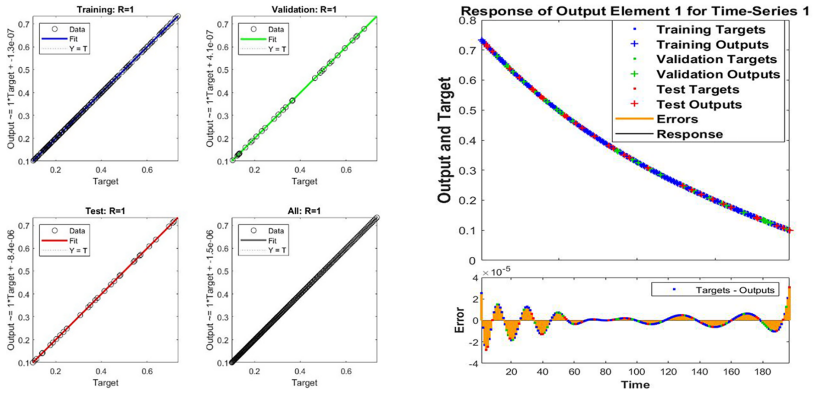

(c). Regression (d). Time Series Response

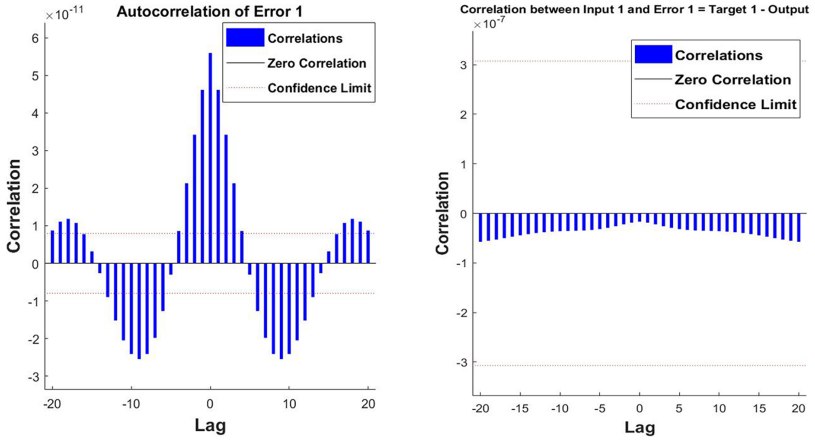

(e). Error Autocorrelation (f). Input Error Cross Correlation

Figure 4: (**a**–**f**): Performance of ANN-NARX for scenario II.

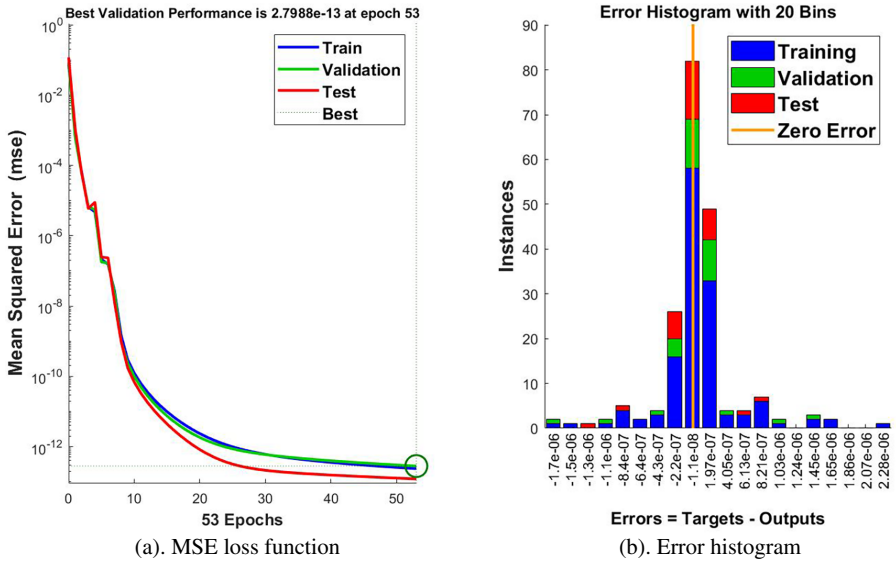

(a). MSE loss function (b). Error histogram

Figure 5: (Continued)

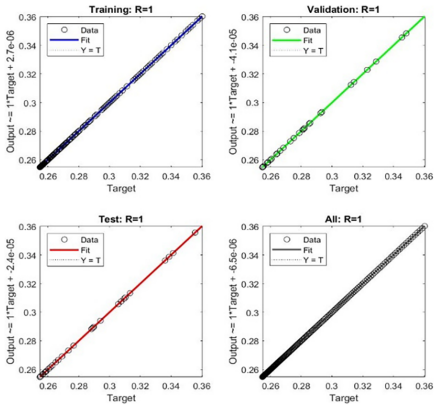

(c). Regression

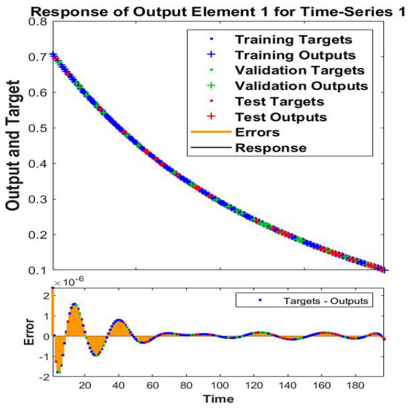

(d). Time Series Response

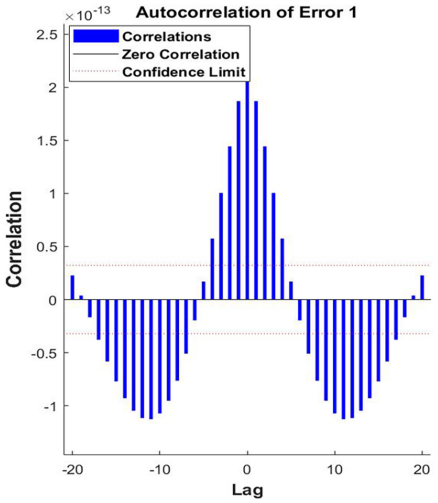

(e). Error Autocorrelation

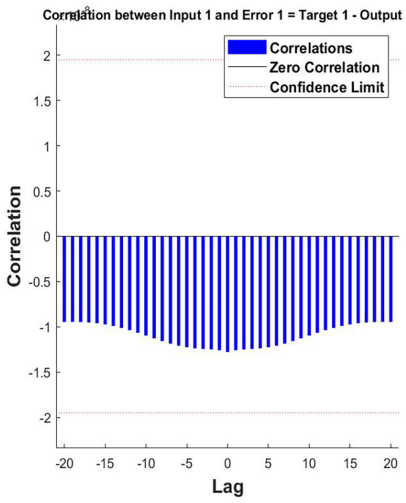

(f). Input Error Cross Correlation

Figure 5: (**a**–**f**): Performance of ANN-NARX for scenario III.

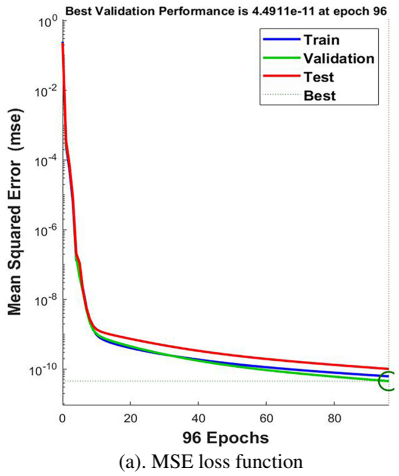

(a). MSE loss function

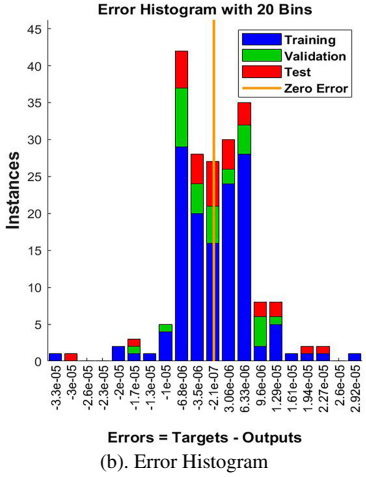

(b). Error Histogram

Figure 6: (Continued)

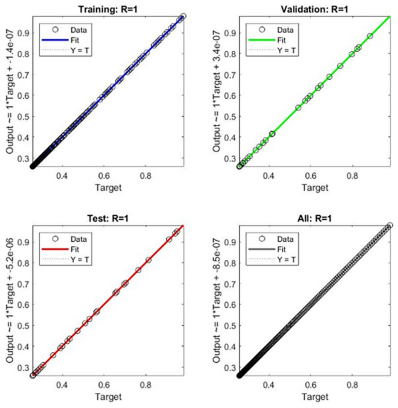

(c). Regression

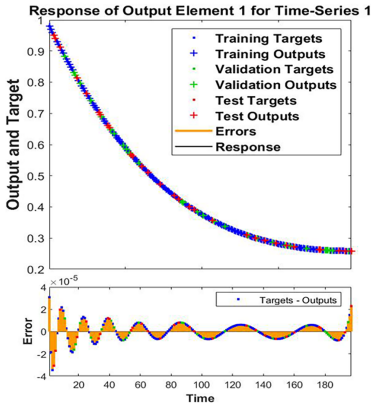

(d). Time Series Response

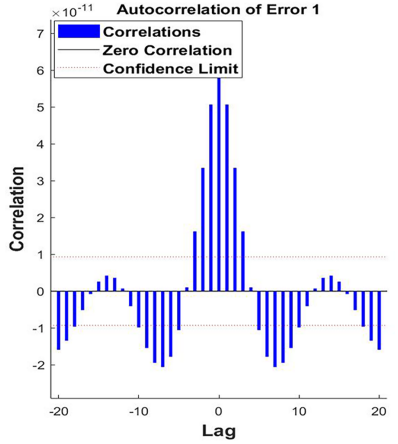

(e). Error Autocorrelation

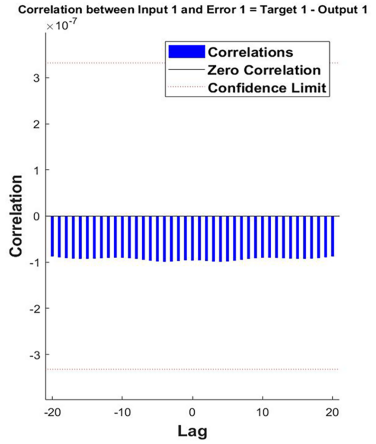

(f). Input Error Cross Correlation

Figure 6: (**a**–**f**): Performance of ANN-NARX for scenario IV.

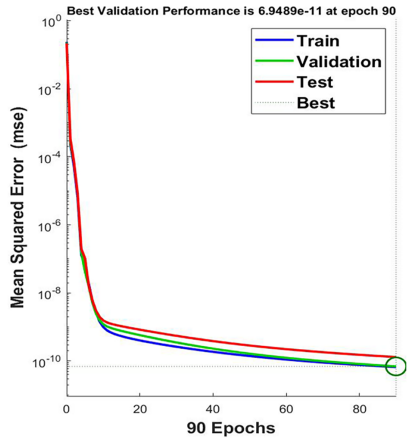

(a). MSE loss function

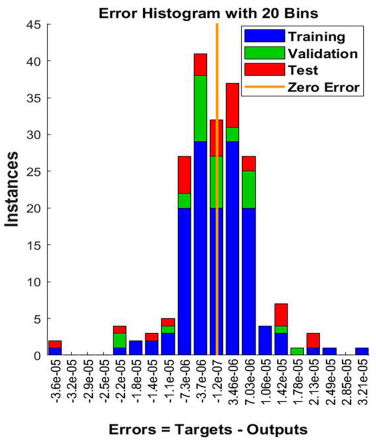

(b). Error Histogram

Figure 7: (Continued)

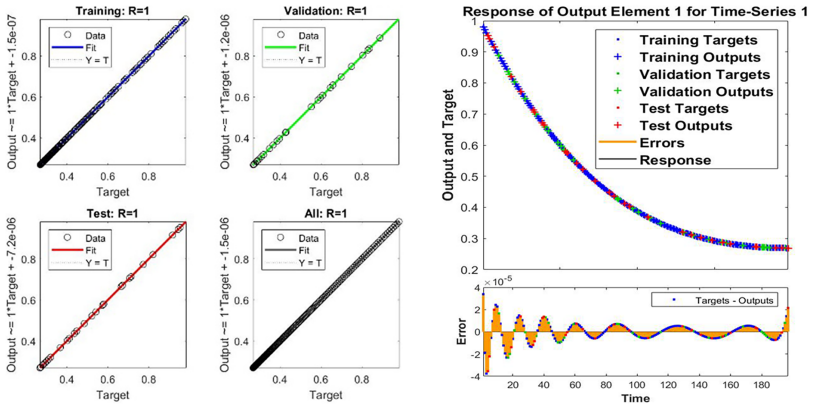

(c). Regression (d). Time Series Response

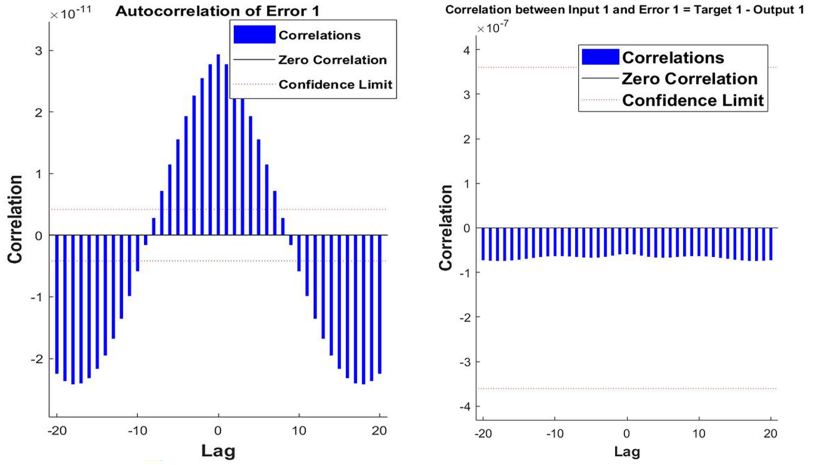

(e). Error Autocorrelation (f). Input Error Cross Correlation

Figure 7: (**a**–**f**): Performance of ANN-NARX for scenario V.

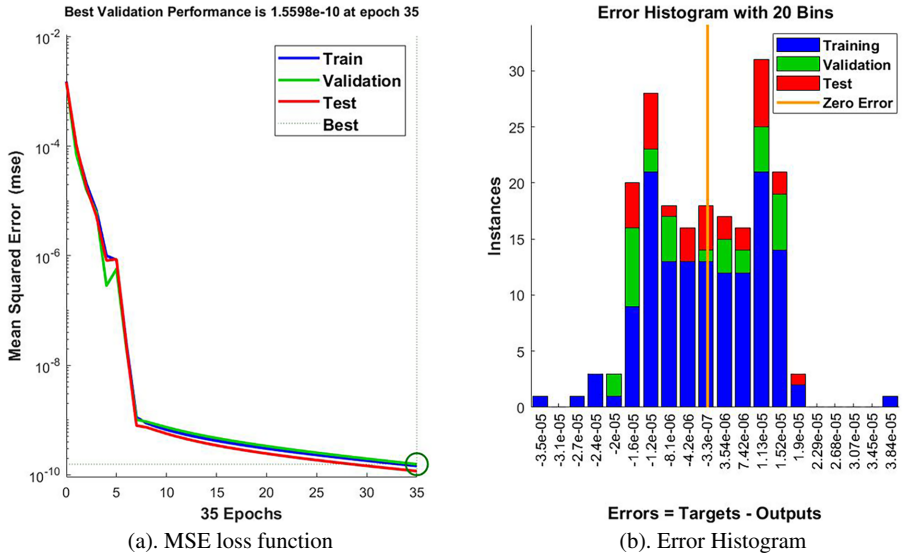

(a). MSE loss function (b). Error Histogram

Figure 8: (Continued)

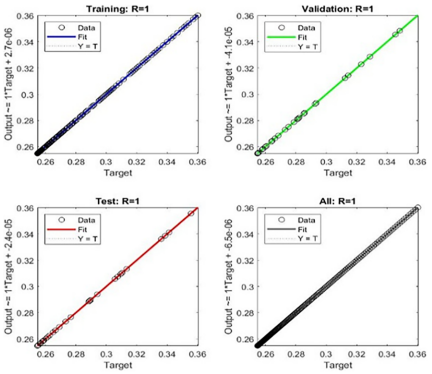

(c). Regression

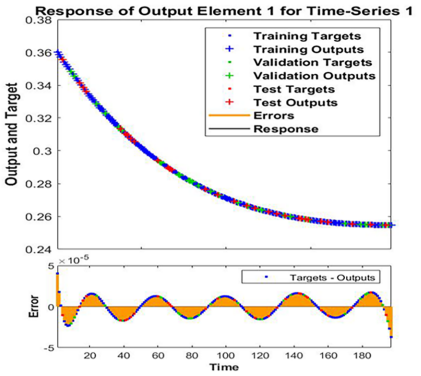

(d). Time Series Response

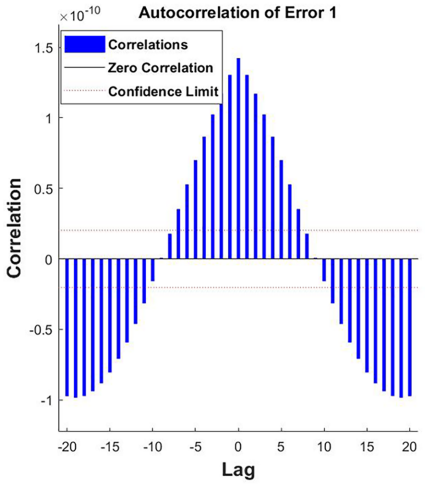

(e). Error Autocorrelation

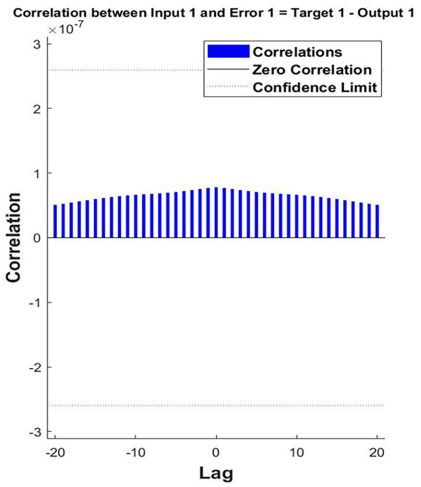

(f). Input Error Cross Correlation

Figure 8: (**a**–**f**): Performance of ANN-NARX for scenario VI.

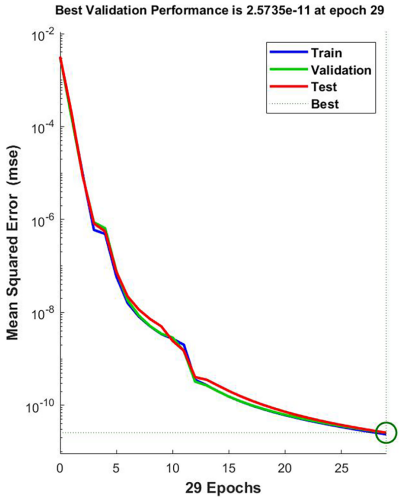

(a). MSE loss function

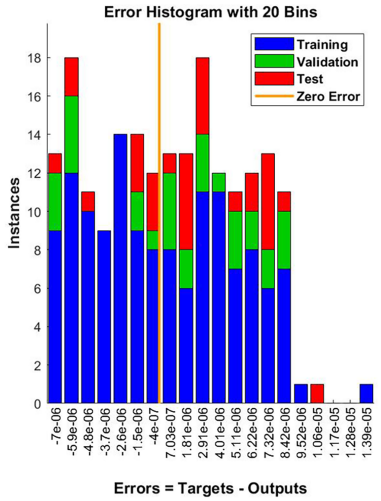

(b). Error Histogram

Figure 9: (Continued)

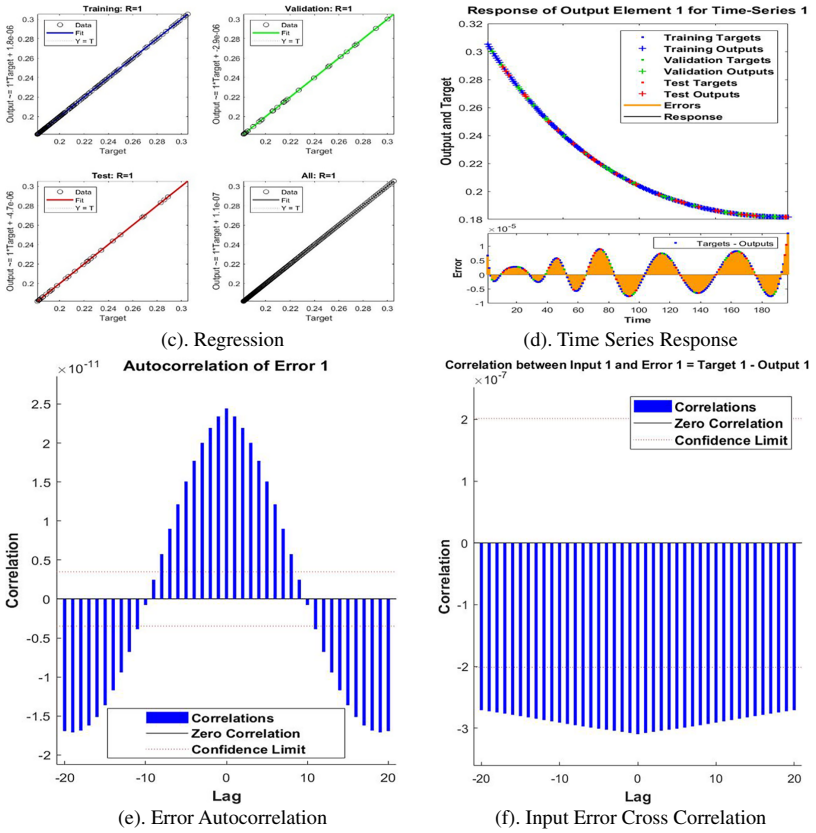

(c). Regression (d). Time Series Response

(e). Error Autocorrelation (f). Input Error Cross Correlation

Figure 9: (**a**–**f**): Performance of ANN-NARX for scenario VII.

4.2 Error Histogram Plot

An error histogram plot in the ANN-NARX model is a visual representation employed to assess the magnitude of errors made by the algorithm on datasets, often the training, validation, and testing data. Figs. 3b–9b especially analyze the error distribution by histogram representation. The 20 bin is adjacent to the zero-error line at 9.81×10^{-8}, 2.29×10^{-7}, 1.10×10^{-8}, -2.10×10^{-7}, -3.3×10^{-7}, -2.025×10^{-7}, and -4.0×10^{-7} for seven distinct situations of ANN-NARX. The error histogram shows that the model is performing well and that there is minimal bias because the errors are primarily grouped around zero. Error histograms use bars from the zero-percent error line to show error dispersion. The 20-bin error histogram shows how prediction mistakes are distributed across ranges. Because the bars are closely packed around zero, the model's predictions are frequently correct. The model is ideally well fitted, according to the distribution, which shows less fluctuation in the error values for the eight scenarios.

4.3 Regression Plots

The prediction diagrams illustrate the fluctuation of the objective and anticipated results in relation to a regression function. The econometric assessment is illustrated in Figs. 3c–9c. The correlated factor $\left(R^2\right)$ is nearly equal to 1, signifying excellent modelling methodology. This substantiates the effectiveness of the suggested ANN-NARX approach in adeptly duplicating SNFFM. Each regression graph possesses unique slopes for training, validation, and evaluation. The predictions of the ANN-NARX are illustrated on the y-axis, whereas the target values are depicted on the x-axis. The results and metrics for each instance during instruction and assessment corresponded with the designated unit values.

4.4 Time Series Response

A time series graph assists in examining time-related structures intrinsic to a model's execution, hence facilitating the observation of performance variations. Figs. 3d–9d display time series charts that facilitate the visualization of temporal patterns and actions. The error levels achieved for the evaluation, training, and validating metrics by the suggested method ANN-NARX are around 2×10^{-5}, 4×10^{-5}, 2×10^{-6}, 4×10^{-5}, 4×10^{-5}, 5×10^{-5} and 1×10^{-5} across seven distinct situations of ANN-NARX. Consistently low errors over the whole computational domain demonstrate the model's good generalization beyond the training data.

4.5 Error Auto-Correlation and Input Error Cross-Correlation Graphs

An input error due to cross-correlation coupled with an error from autocorrelation. Diagrams of ANN-NARX are utilised to analyse the persistent or variable characteristics of prediction errors in contexts including time series or sequential data challenges. This graph is crucial for evaluating the presence of error intersections inside the framework or the emergence of error patterns over a period. The error chart depicts the variance between expected and actual outcomes, facilitating an assessment of the model's reliability. Figs. 3e,f–9e,f analyse the sequential dependencies in errors by error self-correlating and input defect intersection, respectively. The visual representations augment the overall understanding of the investigation study and facilitate precise evaluation of the model's efficacy.

The lack of substantial correlation spikes demonstrates that the residuals are random and that no dynamics remain unlearned.

4.6 Impact of Parameters on Velocity, Temperature, and Concentration

Figs. 10a,b–12a,b display the comparison of numerical and ANN-NARX results for the influence of Helmholtz-Smoluchowski velocity (Uhs), magnetic parameter (M), and porosity parameter (Kp) on velocity distribution, along with their absolute errors (AE). Fluid velocity decreases in accordance with Uhs, (as this characteristic is intimately associated with electrostatic motion), as demonstrated in Fig. 10a. The Uhs quantifies the fluid's velocity in response to an applied electric field when electrified surfaces are engaged. As the flow rate increases, the electro-osmotic driving force intensifies, optimising the overall fluid movement inside the system. The Uhs refers to the speed of a fluid induced by an external electric field in the vicinity of charged surfaces. The viscosity of a fluid is inversely related to the Helmholtz-Smoluchowski velocity, whereas fluid permittivity, zeta potential, and the applied electric field exhibit direct correlations. A diminished electric field, lowered zeta potential, or increased viscosity leads to a decreasing electro-osmotic body force, resulting in decreased fluid flow velocities. The reduction in velocity diminishes the electrostatic driving force, hence decreasing the overall fluid motion within the system. This adjustable electro-osmotic retardation provides a contactless flow control mechanism, making it perfect for microfluidic and lab-on-chip applications. Fig. 11a illustrates the effects of Kp on the velocity profile. Increasing the porosity factor suggests a reduction in the velocity pattern within the motion of a fluid, meaning that as the permeability of a medium increases, the fluid velocity is likely to decrease; simply put, higher pore space provides more obstacles to fluid movement. Increased porosity decreases average velocity by expanding the fluid's flow channels and spreading the same volumetric flux across a larger cross-sectional area. When porosity is increased without increasing permeability, it causes increased tortuosity and drag, which restricts the flow in subsurface systems such as reservoirs or aquifers. Velocity reduction is critical in processes requiring high flow efficiency, such as hydrocarbon recovery, groundwater remediation, and industrial filtering. The decrease in velocity as porosity increases corresponds to an increase in drag in porous media, which is an important component in groundwater cleanup and increased oil recovery. Larger M values lead to a reduced velocity profile, displayed in Fig. 12a. Electric currents are induced in the electrically conducting

fluid as a result of interactions between the magnetic field and the fluid. These currents produce heat as they flow over resistance, raising the fluid's temperature. The strength of the applied transverse magnetic field is represented by the magnetic parameter. The Lorentz force, a resistive body force that opposes fluid motion, becomes stronger as M grows. The fluid is immediately slowed down by this Lorentz force, which operates in the opposite direction of the flow. As a consequence, the velocity profile across the domain is reduced as the velocity boundary layer thickness decreases. The Lorentz force slows the flow while also raising the temperature, a dual effect that may be used in magnetic hyperthermia and electromagnetic braking. This could be attributed to magnetic fields stimulating fluid flow. The magnetic field intensifies with rising M. As an outcome, this feature has a greater impact on fluid dynamics, leading to a narrower velocity distribution. Figs. 10b–12b illustrate the AEs between ANN-NARX prediction and bvp4c reference solutions for velocity profiles. The AE varies from roughly 10^{-3} at the sheet surface $(\eta = 0)$ to below 10^{-7} in the outer flow area $(\eta \to \beta = 1)$. The greatest error arises along the wall, where velocity gradients are most pronounced and boundary layer dynamics are most intricate. Nonetheless, the greatest AE of 10^{-3} signifies a relative error of less than 0.1% for standard velocity magnitudes, so affirming that the ANN-NARX model delivers engineering-level precision for flow field predictions. The rapid attenuation of AE from the wall illustrates that the network effectively encapsulates the asymptotic characteristics of the boundary layer. The ANN-NARX is confirmed as a reliable and effective alternative to traditional numerical methods due to its outstanding, strong performance and accuracy.

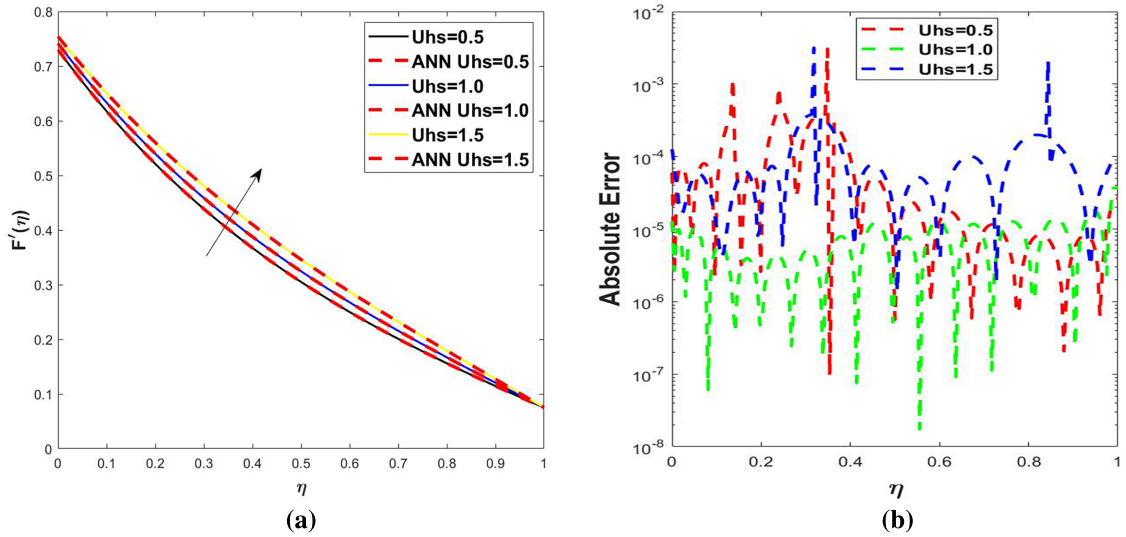

Figure 10: (**a**): Evaluation of proposed ANN-NARX with the numerical reference results and (**b**) AE plot for scenario I.

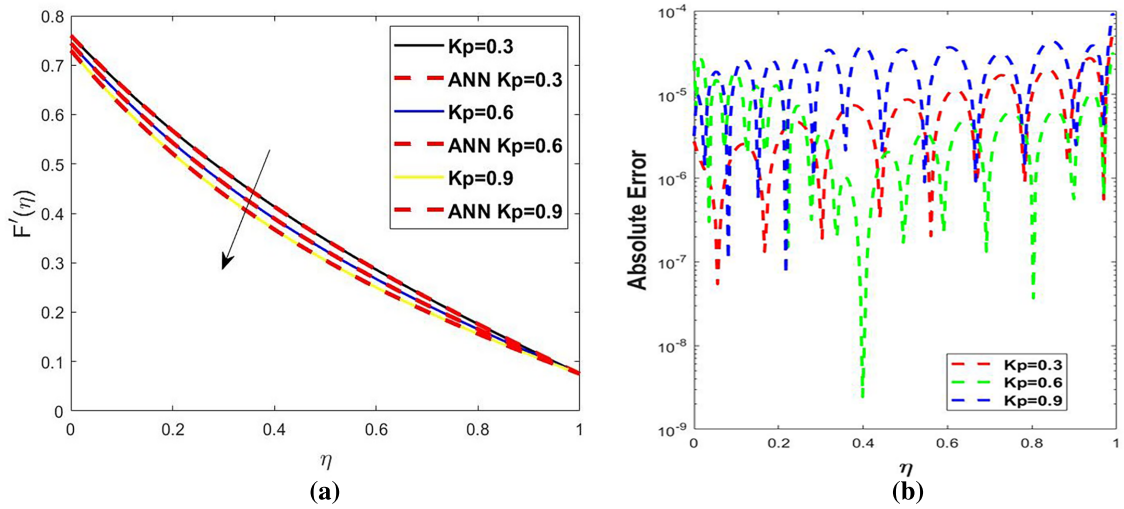

Figure 11: (**a**): Evaluation of proposed ANN-NARX with the numerical reference results and (**b**) AE plot for scenario II.

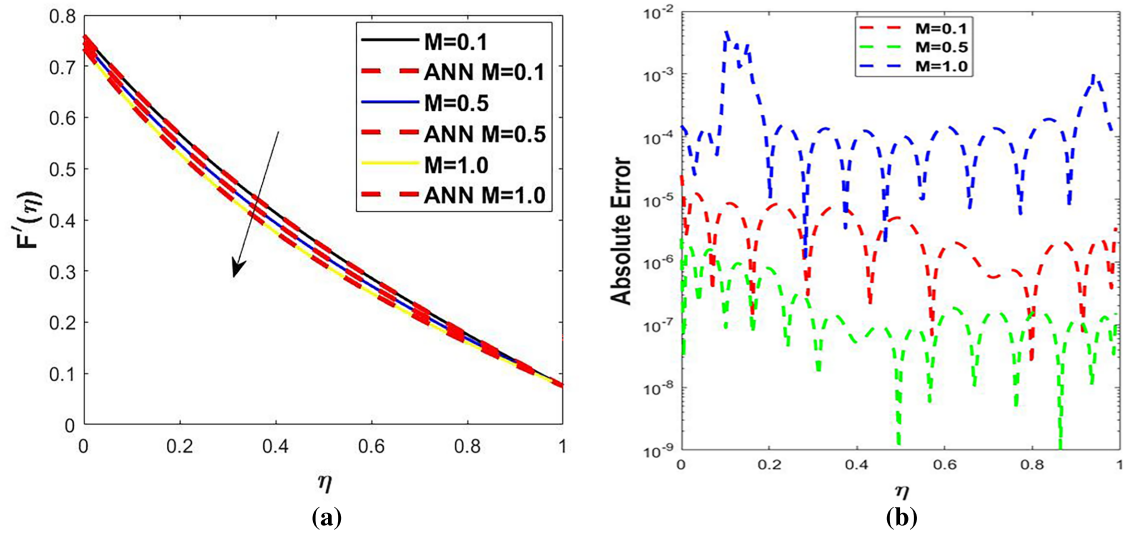

Figure 12: (**a**): Evaluation of proposed ANN-NARX with the numerical reference results and (**b**) AE plot for scenario III.

An examination of the ANN-NARX and numerical findings for θ_w and β_s on the temperature profile, together with their respective AEs, is shown in Figs. 13a,b and 14a,b, respectively. A larger value of θ_w produces a temperature surge, as illustrated in Fig. 13a. When $\theta_w = 1$ the normal radiation-effected flow is restored. In chaotic radiant flow, a temperature boundary layer forms when the interface temperature exceeds the surrounding air temperature. As the external temperature approaches the ambient air temperature, the harmful effects of radiation intensify. Increased radiative heating at greater θ_w speeds up thermal processes and improves energy efficiency in furnaces and solar collectors. A radiative component accelerates small particle movement by causing collisions and converting frictional energy into thermal energy. In all circumstances, nanofluids consistently have a higher temperature than regular fluids. Temperature is boosted against a better approximation of β_s, as depicted in Fig. 14a. When β_s grows, so does the thermal boundary layer (BL) thickness, which leads to increased heat transport. Increasing the thermal BL thickness

β_s improves heat transmission, which is a key principle in modern heat exchanger design. Figs. 13b and 14b illustrate the AE corresponding to temperature profiles for θ_w and β_s, respectively. Errors vary from 10^{-5} next to the heated sheet to 10^{-7} in the free stream. θ_w error ranges from 10^{-5} to 10^{-8}. The somewhat elevated AE in relation to temperature predictions indicates the increased complexity of nonlinear radiation and variable thermal conductivity effects. Nonetheless, an AE of β_s ranges from 10^{-5} to 10^{-7} equating to a temperature deviation of around 0.001°C under standard working conditions, well under permissible thresholds for the majority of thermal engineering applications, such as solar collectors and electronic cooling systems. The model maintains this accuracy throughout the whole spectrum of θ_w and β_s values, indicating strong generalisation.

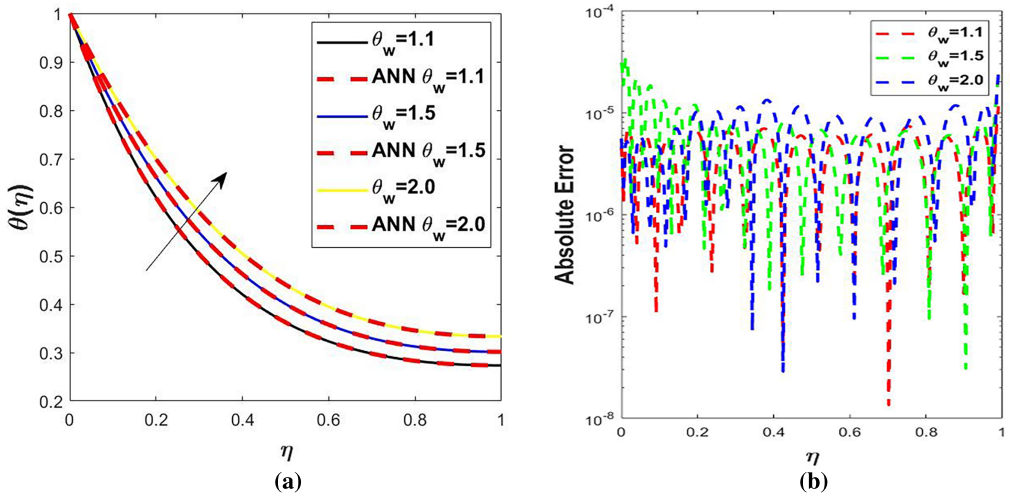

Figure 13: (**a**): Evaluation of proposed ANN-NARX with the numerical reference results and (**b**) AE plot for scenario IV.

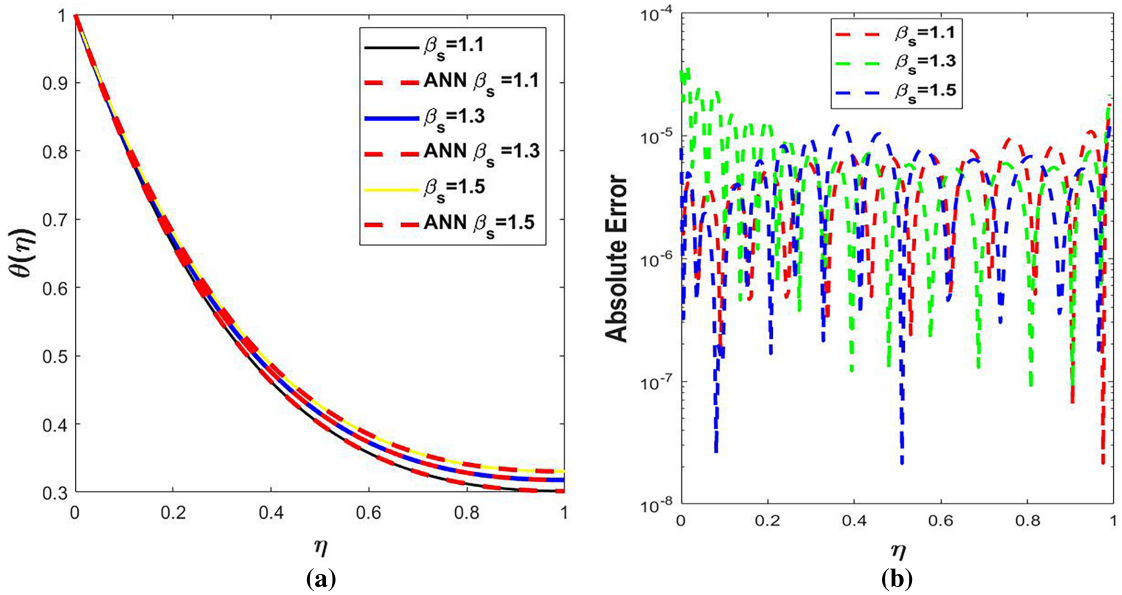

Figure 14: (**a**): Evaluation of proposed ANN-NARX with the numerical reference results and (**b**) AE plot for scenario V.

Fig. 15a depicts the effects of S. As S values rise, the concentration profile diminishes. As S grows, the film thickness diminishes more quickly over time. The temporal thinning of the liquid layer has a more pronounced compressive influence on species movement. As a result, the residence period of nanoparticles and dissolved species in the boundary layer is reduced, limiting the duration for bulk diffusion from the sheet surface. The thinning film intensifies the concentration gradient near the wall due to the reduction of the accessible spatial domain, while the overall concentration profile diminishes as the species are efficiently expelled from the contracting film area. This behaviour is crucial in coating and thin-film manufacturing processes, since elevated unsteady parameters result in accelerated drying or solidification, thereby diminishing the final concentration BL thickness and the overall species distribution within the film. The disparity between the ANN-NARX predictions and the reference numerical solutions is approximately 10^{-4} to 10^{-7}, a notably narrow range that validates the model's exceptional accuracy, stability, and generalisation ability in predicting concentration profiles under diverse S conditions. The little increased inaccuracy along the wall is anticipated and acceptable for engineering purposes, but the swift attenuation away from the wall demonstrates that the network has accurately assimilated the physics of the concentration BL. Fig. 16a illustrates the impact of Sc on fluid density. The Sc will decrease as mass transfer surpasses momentum diffusion, indicating that lower Sc values during fluid movement will be more affected by momentum diffusivity. When the Sc is elevated, momentum diffusion predominates over mass diffusion, signifying that the fluid's viscosity exerts a more significant influence than species diffusion. The momentum diffusivity of fluids with a high Sc ($Sc > 1$), such as lubricants or viscous liquids, significantly exceeds the mass diffusion. Consequently, the transmission of concentration propagates more quickly than momentum as it traverses the fluid. At elevated Sc, energy dispersion, mass transmission is more critical than at lower energy dispersion. The higher concentration layer at high Sc emphasizes momentum diffusion's supremacy over mass diffusion, which is important for constructing chemical vapor deposition and membrane filtering systems. The AE for Sc ranges from 10^{-4} to 10^{-7}, as illustrated in Fig. 16b. The AE plot shows a maximum prediction error of 10^{-4} near the sheet, which corresponds to the region with the biggest velocity and temperature gradients. This is to be expected given the complexity of the physics there. The ANN-NARX model delivers excellent accuracy and outstanding stability over the computational domain, ensuring dependable engineering predictions. The error decays fast to as low as 10^{-7} away from the boundary.

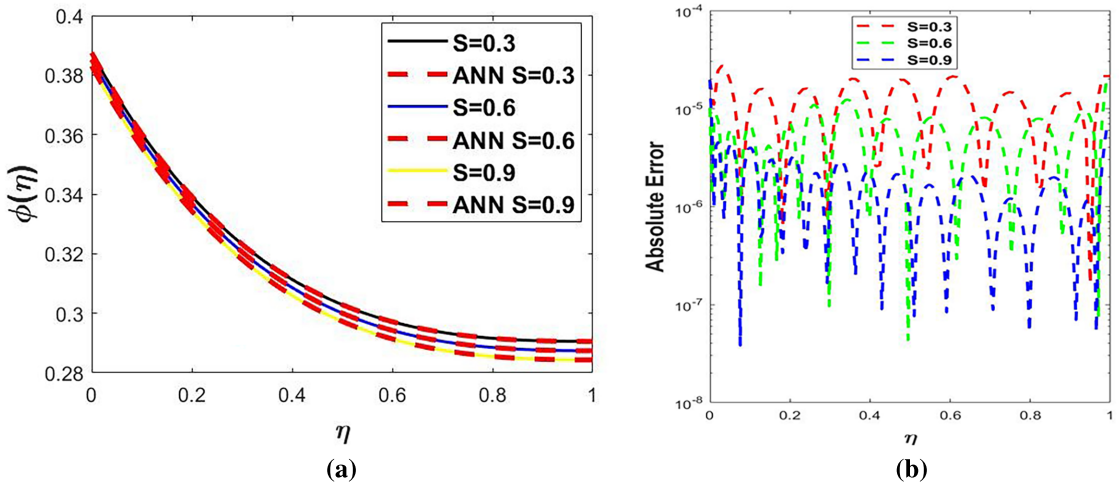

Figure 15: (**a**): Evaluation of proposed ANN-NARX with the numerical reference results and (**b**) AE plot for scenario VI.

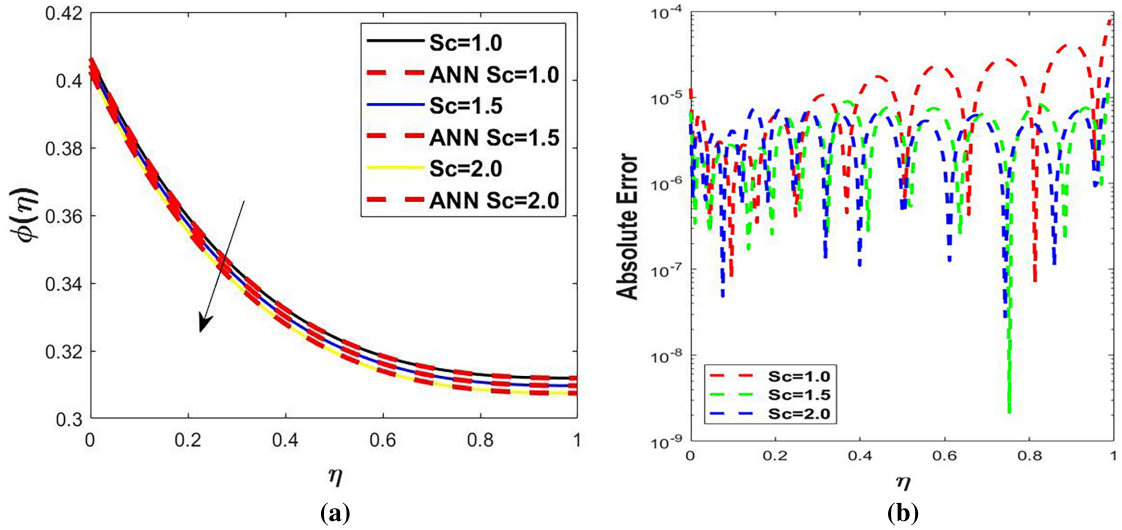

Figure 16: (**a**): Evaluation of proposed ANN-NARX with the numerical reference results and (**b**) AE plot for scenario VII.

Table 6 shows the network performance for Scenarios I to VII, encompassing training, validation, and testing MSE loss function along with performance, gradient, mu, epoch count, and calculation time. The least MSE was attained under many circumstances and epochs for every scenario shown in the findings. Consistently low MSE values across all situations support the prediction accuracy and general strength of the model. In particular, Scenario VI demonstrates the lowest MSE in instance 1 after only a few epochs, highlighting the model's effectiveness in quickly converging to an optimal solution. Every scenario shows regression values (*R*-squared) near equal to 1, therefore suggesting a perfect match between expected and real outcomes. The computation time is still effective; in all cases, it only takes two seconds maximum. Variations in Mu and gradient values among various scenarios also help further boost the adaptive learning capability and training stability of the model. These results confirmed the excellent performance and rapid convergence of the LMT-NNA model throughout a spectrum of input circumstances.

Table 6: Outcomes of ANN-NARX for scenarios I to VIII.

Scenario	MSE			Performance	Gradient	Mu	Epoch	Time (s)
	Training	Validation	Testing					
I	6.69E−11	8.29E−11	6.86E−11	6.69E−11	9. 58E−8	1.00E−08	79	02
II	4.46E−10	5.63E−11	1.07E−10	4.46E−11	9. 85E−8	1.00E−08	79	02
III	2.37E−13	2.79E−13	1.21E−13	2.37E−13	9. 58E−8	1.00E−10	53	02
VI	6.18E−11	4.49E−11	1.01E−10	6.18E−11	9. 99E−8	1.00E−08	96	03
V	1.31E−11	6.94E−11	1.31E−10	6.66E−11	9. 76E−8	1.00E−08	90	02
VI	1.44E−10	1.55E−10	1.16E−10	1.45E−10	9. 90E−8	1.00E−08	35	02
VII	2.38E−11	2.57E−11	2.58E−11	2.38E−11	9. 11E−8	1.00E−09	29	02

Table 7 illustrates the efficacy of the factors Uhs, Kp, M, θ_w, β_s, S, and Sc in terms of skin friction coefficient, Nusselt number, and Sherwood number. Greater values of Uhs and θ_w diminish the coefficient of skin friction, while the M, Kp, S, and Schmidt number Sc have a contrasting effect. The heat transfer rate,

represented by the Nusselt number, decreases as θ_w, Kp, M and β_s increase. On the other hand, higher values of Uhs, S and Sc increase the Nusselt number, indicating enhanced heat transfer. The Sherwood number, associated with mass transfer, is positively influenced by S and Sc, while higher Sc generally reduces it slightly due to thicker concentration BLs.

Table 7: Numerical results of skin friction, Nusselt number, and Sherwood number.

Uhs	Kp	M	θ_w	β_s	S	Sc	Skin Friction	Nusselt Number	Sherwood Number
0.5	0.4	0.3	0.2	0.3	0.5	0.5	−1.65060572	5.28317104	0.41268804
1.0	0.4	0.3	0.2	0.3	0.5	0.5	−1.56229137	5.33256170	0.41308908
1.5	0.4	0.3	0.2	0.3	0.5	0.5	−1.51328058	5.37722806	0.41348049
0.2	0.3	0.3	0.2	0.3	0.5	0.5	−1.51328058	5.29245021	0.41277274
0.2	0.6	0.3	0.2	0.3	0.5	0.5	−1.58435830	5.21313684	0.41215623
0.2	0.9	0.3	0.2	0.3	0.5	0.5	−1.65194549	5.12899356	0.41155468
0.2	0.4	0.1	0.2	0.3	0.5	0.5	−1.48107321	5.91814282	0.41349559
0.2	0.4	0.5	0.2	0.3	0.5	0.5	−1.56106793	5.05758550	0.41226189
0.2	0.4	1.0	0.2	0.3	0.5	0.5	−1.74386897	4.06901401	0.41078919
0.2	0.4	0.3	1.1	0.3	0.5	0.5	−1.56097425	5.47963763	0.41287236
0.2	0.4	0.3	1.3	0.3	0.5	0.5	−1.54146599	3.85293131	0.41182116
0.2	0.4	0.3	1.5	0.3	0.5	0.5	−1.52761030	2.90287358	0.41122151
0.2	0.4	0.3	0.2	1.1	0.5	0.5	−1.53568861	5.43289038	0.41287939
0.2	0.4	0.3	0.2	1.5	0.5	0.5	−1.52768492	5.34405721	0.41290818
0.2	0.4	0.3	0.2	2.0	0.5	0.5	−1.51872698	5.27319170	0.41293956
0.2	0.4	0.3	0.2	0.3	0.3	0.5	−1.55489160	4.81735474	0.38347202
0.2	0.4	0.3	0.2	0.3	0.6	0.5	−1.52748577	5.11687859	0.40059298
0.2	0.4	0.3	0.2	0.3	0.9	0.5	−1.47747765	5.36199901	0.41039751
0.2	0.4	0.3	0.2	0.3	0.5	1.1	−1.40339108	5.44434434	0.38140209
0.2	0.4	0.3	0.2	0.3	0.5	1.5	−1.40849998	5.43776923	0.39904109
0.2	0.4	0.3	0.2	0.3	0.5	2.0	−1.41232822	5.43289038	0.41287939

5 Conclusions

This study discusses the computational solution of unsteady, mixed convection, two-dimensional movement of an electro-osmotic Sutterby hybrid (AA7075 + AA7072/SA) nanofluidic thin film flow model across a porous inclined sheet, employing NARX artificial intelligence multilayer algorithm known as ANN-NARX in conjunction with LMA. The test data constitutes 10% of the reference data set, with an additional 10% allocated for validation, while the remaining 80% is designated for training data. The effects of variable thermal conductivity, nonlinear thermal radiation, melting heat, and Newtonian heating are discussed in this article, and it provides major insights into advanced thermal problems. The Darcy model incorporates the effects of porosity and inertial resistance to model how a porous material affects a process. The method of this distribution is aimed at enhancing the accuracy of modeling and enabling a fair evaluation of results attained in optimal approximation. The results of this current research provide major insights into physical fluid model descriptions, as discussed below:

- The stability, reliability, and trustworthiness of the suggested approach are well supported by ANN-NARX studies, which also validate its choice as the best course of action for the suggested model. In

the given scenario, the method's accuracy, efficacy, and dependability are shown by the lowest absolute error value (10^{-3} to 10^{-8}) that was attained. A loss function (MSE) lies in the interval of 10^{-10} to 10^{-13}, error histogram ranges between 10^{-07} to 10^{-08}, and R^2 close to 1 in all scenarios. This is indicative of excellent prediction accuracy and a strong fit to real data, according to performance metrics.

- Time series analysis, autocorrelation tests, and correlation studies were among the convergence methods used to examine the adaptability and effectiveness of nonlinear autoregressive exogenous neural models. Complex time series dynamics, autocorrelation, and correlation tests were successfully handled by the computational approach.
- The Mu ranges between 10^{-08} to 10^{-10}, while the gradient lies near 10^{-08}.
- Increasing Kp and M values for the fluid model leads to a drop in the velocity profile, whereas increasing the values for Uhs.
- The temperature gradients show that as θ_w and β_s values grow, the thickness of the thermal boundary layer is also affected.
- As S and Sc values grow, the concentration profile diminishes.
- The skin friction coefficient is affected by β_s pseudoplastic properties and Uhs. As the Sutterby fluid parameter and Uhs increase, it affects the distribution of surface stress and decreases the wall shear stress, while skin friction improves with an increase of Kp.
- The electric double layer (EDL) becomes more active and improves fluid movement close to the wall as Uhs parameter is raised. As flow velocity increases, thermal boundary layers are reduced, improving wall temperature gradients and raising the wall heat flux while declining for Kp and β_s.

Future Work

Future investigations may enhance and broaden the Heuristic-physics-informed neural network (H-PINN) framework. Quantum-PINNs (Q-PINNs) have the potential to expedite computations and facilitate the resolution of intricate fluid systems by using specialised optimizers derived from quantum mechanics, in conjunction with multi-phase flows, reactive flows involving complicated fluid dynamics, bio-fluid, drilling fluid, and chemistry applications. Bayesian PINNs and other techniques for quantifying uncertainty may facilitate result prediction and reliability assessment in the context of noisy data and variable factors in industrial design and safety.

Limitations

Although this work models a complex Sutterby hybrid nanofluid system using an inventive use of ANN, there are a number of limitations that need to be noted. The enquiry is entirely computational and lacks experimental confirmation, which is the first and most important point. The reported exceptional accuracy (R^2 = 0.999, MSE as low as 10^{-13}) only confirms that the ANN successfully replicates the numerical model, not that the numerical model itself accurately represents the actual physical behaviour of AA7075/AA7072 nanoparticles suspended in sodium alginate. This is because the ANN was trained solely on synthetic data produced by MATLAB's bvp4c numerical solver. There is no comparison with established experimental standards or laboratory measures.

Acknowledgement: The Researchers would like to thank the Deanship of Graduate Studies and Scientific Research at Qassim University for financial support (QU-APC-2026).

Funding Statement: The APC was funded by the Deanship of Graduate Studies and Scientific Research at Qassim University (QU-APC-2026).

Author Contributions: The authors confirm contribution to the paper as follows: Conceptualization, Muhammad Nadeem and Imran Siddique; methodology, Zohaib Zahid and Imran Siddique; software, Irfan Saif Ud Din, Muhammad

Nadeem and Ibrahim Alraddadi; validation, Imran Siddique and Taha Radwan; formal analysis, Zohaib Zahid, Muhammad Nadeem and Ibrahim Alraddadi; investigation, Muhammad Nadeem; data curation, Taha Radwan and Irfan Saif Ud Din; writing—original draft preparation, Irfan Saif Ud Din, Muhammad Nadeem and Zohaib Zahid; writing—review and editing, Imran Siddique, Ibrahim Alraddadi and Taha Radwan; visualization, Zohaib Zahid and Muhammad Nadeem; supervision, Imran Siddique; project administration, Imran Siddique and Taha Radwan; funding acquisition, Taha Radwan. All authors reviewed and approved the final version of the manuscript.

Availability of Data and Materials: All data generated or analyzed during this study are included in this manuscript.

Ethics Approval: Not applicable.

Conflicts of Interest: The authors declare no conflicts of interest.

References

1. Nour MM, Tony MA, Nabwey HA. Nanomaterials and nanofluids for environmental applications: a comprehensive review. J Eng. 2026;2026(1):3370145. doi:10.1155/je/3370145.
2. Madhu J, Madhukesh JK, Sarris I, Prasannakumara BC, Ramesh GK, Ali Shah N, et al. Influence of quadratic thermal radiation and activation energy impacts over oblique stagnation point hybrid nanofluid flow across a cylinder. Case Stud Therm Eng. 2024;60(9):104624. doi:10.1016/j.csite.2024.104624.
3. Choi SU, Eastman JA. Enhancing thermal conductivity of fluids with nanoparticles. In: ASME 1995 International Mechanical Engineering Congress and Exposition; 1995 Nov 12–17; San Francisco, CA, USA.
4. Sajid T, Jamshed W, Shahzad F, Akgül EK, Nisar KS, Eid MR. Impact of gold nanoparticles along with Maxwell velocity and Smoluchowski temperature slip boundary conditions on fluid flow: sutterby model. Chin J Phys. 2022;77(2):1387–404. doi:10.1016/j.cjph.2021.11.011.
5. Ali Khan L, Raza M, Ahmad Mir N, Ellahi R. Effects of different shapes of nanoparticles on peristaltic flow of MHD nanofluids filled in an asymmetric channel. J Therm Anal Calorim. 2020;140(3):879–90. doi:10.1007/s10973-019-08348-9.
6. Cao W, Animasaun IL, Yook SJ, Oladipupo VA, Ji X. Simulation of the dynamics of colloidal mixture of water with various nanoparticles at different levels of partial slip: ternary-hybrid nanofluid. Int Commun Heat Mass Transf. 2022;135(9):106069. doi:10.1016/j.icheatmasstransfer.2022.106069.
7. Alfellag MA, Kamar HM, Sidik NAC, Muhsan AS, Kazi SN, Alawi OA, et al. Rheological and thermophysical properties of hybrid nanofluids and their application in flat-plate solar collectors: a comprehensive review. J Therm Anal Calorim. 2023;148(14):6645–86. doi:10.1007/s10973-023-12184-3.
8. Farooq N, Hussain A, Sarwar L, Nadeem M, Ahmad A. Case study of heat flux conveying the engine oil/(ZnO + MoS_2) hybrid nanoparticles via permeable wedge-shaped geometry: heat source-sink and electroosmosis applications. ZAMM J Appl Math Mech/Z Angew Math Mech. 2025;105(10):e70255. doi:10.1002/zamm.70255.
9. Afridi MI, Riasat S, Iqbal S, Bilal S, Alderremy AA, Mahmoud EE. Nanocomposites of various shapes in trihybrid nanofluid flow past a Riga plate with electroosmotic effects. Alex Eng J. 2025;113(3):498–508. doi:10.1016/j.aej.2024.11.043.
10. Jawad M, Khan Z, Bonyah E, Jan R. Analysis of hybrid nanofluid stagnation point flow over a stretching surface with melting heat transfer. Math Probl Eng. 2022;2022:9469164. doi:10.1155/2022/9469164.
11. Nadeem M, Siddique I, Awrejcewicz J, Bilal M. Numerical analysis of a second-grade fuzzy hybrid nanofluid flow and heat transfer over a permeable stretching/shrinking sheet. Sci Rep. 2022;12(1):1631. doi:10.1038/s41598-022-05393-7.
12. Rehman S, Mir NA, Farooq M, Rizwan M, Ahmad F, Ahmad S, et al. Analysis of thermally stratified flow of Sutterby nanofluid with zero mass flux condition. J Mater Res Technol. 2020;9(2):1631–9. doi:10.1016/j.jmrt.2019.11.088.
13. Nawaz M. Role of hybrid nanoparticles in thermal performance of Sutterby fluid, the ethylene glycol. Phys A Stat Mech Appl. 2020;537:122447. doi:10.1016/j.physa.2019.122447.

14. Bilal S, Sohail M, Naz R, Malik MY. Dynamical and optimal procedure to analyze the exhibition of physical attributes imparted by Sutterby magneto-nanofluid in Darcy medium yielded by axially stretched cylinder. Can J Phys. 2020;98(1):1–10. doi:10.1139/cjp-2018-0581.
15. Sabir Z, Imran A, Umar M, Zeb M, Shoaib M, Raja MA. A numerical approach for two-dimensional Sutterby fluid flow bounded at a stagnation point with an inclined magnetic field and thermal radiation impacts. Therm Sci. 2020;186:186. doi:10.2298/tsci191207186s.
16. Song YQ, Waqas H, Al-Khaled K, Farooq U, Ullah Khan S, Khan MI, et al. Bioconvection analysis for Sutterby nanofluid over an axially stretched cylinder with melting heat transfer and variable thermal features: a Marangoni and solutal model. Alex Eng J. 2021;60(5):4663–75. doi:10.1016/j.aej.2021.03.056.
17. Abbasi A, Farooq W, Khan SU, Amer H, Khan MI. Electroosmosis optimized thermal model for peristaltic flow of with Sutterby nanoparticles in asymmetric trapped channel. Eur Phys J Plus. 2021;136(12):1207. doi:10.1140/epjp/s13360-021-02161-w.
18. Hayat T, Ahmad S, Khan MI, Alsaedi A. Modeling chemically reactive flow of sutterby nanofluid by a rotating disk in presence of heat generation/absorption. Commun Theor Phys. 2018;69(5):569. doi:10.1088/0253-6102/69/5/569.
19. Tripathi D, Bhushan S, Bég OA. Transverse magnetic field driven modification in unsteady peristaltic transport with electrical double layer effects. Colloids Surf A Physicochem Eng Aspects. 2016;506:32–9. doi:10.1016/j.colsurfa.2016.06.004.
20. Hafez NM, Thabet EN, Khan Z, Abd-Alla AM, Elhag SH. Electroosmosis-modulated Darcy-Forchheimer flow of Casson nanofluid over stretching sheets in the presence of Newtonian heating. Case Stud Therm Eng. 2024;53:103806. doi:10.1016/j.csite.2023.103806.
21. Narla VK, Tripathi D, Bég OA. Analysis of entropy generation in biomimetic electroosmotic nanofluid pumping through a curved channel with joule dissipation. Therm Sci Eng Prog. 2020;15(3):100424. doi:10.1016/j.tsep.2019.100424.
22. Zaher AZ, Ali KK, Mekheimer KS. Electroosmosis forces EOF driven boundary layer flow for a non-Newtonian fluid with planktonic microorganism: Darcy Forchheimer model. Int J Numer Methods Heat Fluid Flow. 2021;31(8):2534–59. doi:10.1108/HFF-10-2020-0666.
23. Riasat S, Khan SA, Bilal M, Sambas A, Maatki C, Eladeb A, et al. Thermal energy optimization for electroosmotic flow of ternary nanocomposition with Debye-Hückel linearization approach. Case Stud Therm Eng. 2025;69(35):105996. doi:10.1016/j.csite.2025.105996.
24. Nadeem M, Franco AT, Siddique I, Garcia-Blanco YJ, Quitian-Ardila LH, Khan R. Role of electroosmotic and Darcy-Forchheimer Law on magnetohydrodynamic Williamson hybrid nanofluid flow over a moving thin needle. Chaos Solitons Fractals. 2025;192(2):116021. doi:10.1016/j.chaos.2025.116021.
25. Ranjit NK, Shit GC, Tripathi D. Entropy generation and Joule heating of two layered electroosmotic flow in the peristaltically induced micro-channel. Int J Mech Sci. 2019;153:430–44. doi:10.1016/j.ijmecsci.2019.02.022.
26. Bilal M, Ahmad Lone S, Anwar S, Shahab S, Fatima S, Ramzan M, et al. An exact solution for the entropy base flow of electroosmotic magneto-nanofluid through microparallel channel. Int J Mod Phys B. 2025;39:2550003. doi:10.1142/s0217979225500031.
27. Shah Z, Pasha AA, Nasir M, Basingab MS, Zafar M, Hameed AZ, et al. Thermally magnetized Darcy–Forchheimer Eyringen micropolar material subject to chemical kinetics: a machine learning analysis. Chem Eng J Adv. 2026;25(9):100992. doi:10.1016/j.ceja.2025.100992.
28. Ilyas H, Ahmad I, Raja MAZ, Shoaib M. A novel design of Gaussian WaveNets for rotational hybrid nanofluidic flow over a stretching sheet involving thermal radiation. Int Commun Heat Mass Transf. 2021;123(4):105196. doi:10.1016/j.icheatmasstransfer.2021.105196.
29. Zeeshan A, Khan MI, Ellahi R, Marin M. Computational intelligence approach for optimising MHD casson ternary hybrid nanofluid over the shrinking sheet with the effects of radiation. Appl Sci. 2023;13(17):9510. doi:10.3390/app13179510.
30. Sabir Z, Wahab HA, Umar M, Sakar MG, Raja MAZ. Novel design of Morlet wavelet neural network for solving second order Lane-Emden equation. Math Comput Simul. 2020;172:1–14. doi:10.1016/j.matcom.2020.01.005.

31. Uddin I, Ullah I, Raja MAZ, Shoaib M, Islam S, Zobaer MS, et al. The intelligent networks for double-diffusion and MHD analysis of thin film flow over a stretched surface. Sci Rep. 2021;11(1):19239. doi:10.1038/s41598-021-97458-2.
32. Ishaq M, Ashraf MB, Alhudhaibi AM, Jari H, Altherwi AA, Faqihi AA. TensorFlow-based neural network modeling and thermodynamic optimization of electroosmotic peristaltic flow of a viscoelastic fluid in an asymmetric channel. Int Commun Heat Mass Transf. 2026;175(4):111023. doi:10.1016/j.icheatmasstransfer.2026.111023.
33. Islam T, Jewel Rana BM, Ali MY, Hossain KE, Mukherjee A, Hossain SN, et al. Study of thermo-fluid dynamics of magnetised hybrid nanofluids over a bi-directional surface using ANN-optimization. J Mol Liq. 2026;449:129418. doi:10.1016/j.molliq.2026.129418.
34. Yousuf Ali M, Jewel Rana BM, Islam T, Hossain MS, Parvez MS, Afikuzzaman M. Artificial neural network-assisted modeling of electroosmotic heat transfer in radiative ternary hybrid nanofluid with gyrotactic microorganisms. J Therm Anal Calorim. 2025;150(26):21913–42. doi:10.1007/s10973-025-14859-5.
35. Priyadharshini P, Archana MV, Ali Shah N, Alshehri MH. Ternary hybrid nanofluid flow emerging on a symmetrically stretching sheet optimization with machine learning prediction scheme. Symmetry. 2023;15(6):1225. doi:10.3390/sym15061225.
36. Din ISU, Siddique I, Zahid Z, Nadeem M, Islam S. ANN-based analysis of thin film Maxwell fluid dynamics with electro-osmotic and nonlinear thermal effects. Alex Eng J. 2025;127(5):392–410. doi:10.1016/j.aej.2025.04.084.